Recent advances in gas-involved *in situ* studies via transmission electron microscopy

Ying Jiang[1,2], Zhengfei Zhang[1], Wentao Yuan[1], Xun Zhang[1], Yong Wang[1] (✉), and Ze Zhang[1] (✉)

[1] Center of Electron Microscopy and State Key Laboratory of Silicon Materials, School of Materials Science and Engineering, Zhejiang University, Hangzhou 310027, China
[2] Materials Genome Institute, Shanghai University, Shanghai 200444, China

ABSTRACT

Gases that are widely used in research and industry have a significant effect on both the configuration of solid materials and the evolution of reactive systems. Traditional studies on gas–solid interactions have mostly been static and post-mortem and unsatisfactory for elucidating the real active states during the reactions. Recent developments of controlled-atmosphere transmission electron microscopy (TEM) have led to impressive progress towards the simulation of real-world reaction environments, allowing the atomic-scale recording of dynamic events. In this review, on the basis of the *in situ* research of our group, we outline the principles and features of the controlled-atmosphere TEM techniques and summarize the significant recent progress in the research activities on gas–solid interactions, including nanowire growth, catalysis, and metal failure. Additionally, the challenges and opportunities in the real-time observations on such platform are discussed.

1 Introduction

Gaseous species are extensively involved in most important issues in our daily life, as well as in chemical production [1, 2], automotive exhaust treatment [3, 4], fuel cells [5, 6], gas sensors [7, 8], and metal failure [9, 10]. For a particular material, the structure and chemistry may respond in a complex way to gases during synthesis [11–14], treatment [15–18], and usage [19–21], significantly influencing the physicochemical properties. Therefore, to design and optimize specific functions, it is critical to obtain information about the structure and chemistry evolution in gaseous environments. However, traditional research has mostly been post-mortem or fragmented. Researchers had to interrupt the reaction, remove the sample from the stage, and characterize it, which is time-consuming and does not guarantee the observation of a complete reaction on the same particle. More importantly, the structures characterized via post-mortem methods may not represent the truly active states that emerge during the reactions. To solve these problems, controlled-

🄣 **TSINGHUA** UNIVERSITY PRESS 🙋 Springer

atmosphere transmission electron microscopy (TEM) techniques have been used to identify the metastable and active states down to the atomic scale, obtain thermodynamic and kinetic data, and identify the mechanism whereby the interaction proceeds microscopically.

Since it was invented by Ernst Ruska in 1931, TEM has become a powerful approach for characterizing the surface/bulk structure and composition of materials. In the past decades, *in situ* TEM studies have attracted considerable attention [22], including heating [23–25], electrical-biasing [26–28], and mechanical-loading [29–34] experiments. However, gas-involved experiments are less straightforward, as the gaseous environment obviously runs counter to the requirement of high vacuum within the TEM column (regularly 10^{-6}–10^{-10} Torr). A classical method for closing the pressure gap while maintaining the remarkable resolution of TEM is limiting the gas in the vicinity of the sample. Related attempts date back to 1935, when Marton [35] suggested the modification of either the holders or the objective pole pieces of transmission electron microscopes. In the following decades, both approaches developed rapidly. Numerous articles and book chapters [36–45] have addressed the technical adaptations and major application examples, mainly focusing on catalysis. In addition to catalysis, nanomaterial growth [46–48], metal failure [49, 50], phase transitions [51, 52], and oxidation/reduction reactions [53–59] have been investigated.

In this review, after a brief introduction to the current status of the controlled-atmosphere TEM techniques, we summarize the major recent advances, including nanowire (NW) growth, surface modification, the shape and composition changes of the catalysts, and metal failure. We also discuss the challenges and opportunities of controlled atmosphere TEM on the basis of the problems encountered during the *in situ* experiments, such as the structure resolving, dynamic monitoring, and coupling with other external stimuli.

2 Creating a controlled-atmosphere environment for TEM

Figure 1 shows a schematic of the current controlled-atmosphere TEM technique, as well as some integrated
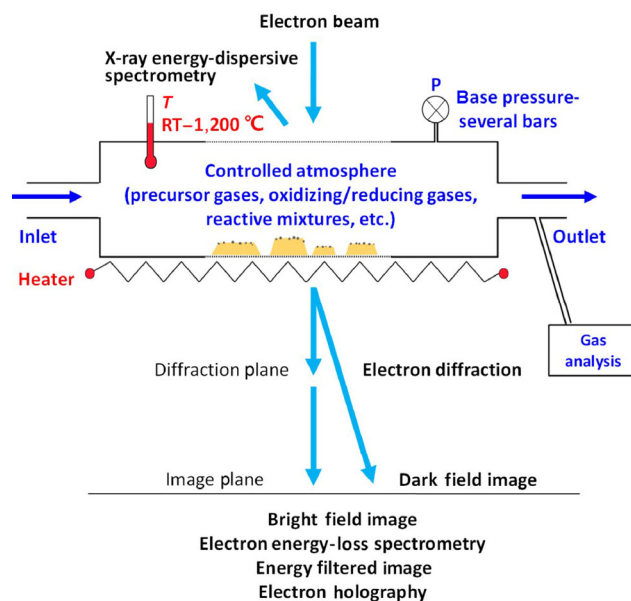

Figure 1 Schematic of the controlled-atmosphere TEM technique and analytical methods.

analytical methods. *In situ* gas-involved experiments require a provision wherein the sample subjected to TEM is surrounded by controlled gas phases, which must be confined to the local region to retain the working state of the transmission electron microscope. To date, two typical approaches have emerged as commercial or custom-designed strategies for the lattice-resolved and pressure-tolerant video-rate recording of the material behavior in gaseous environments: the open type and the closed type.

2.1 Open type

The open-type method is realized using a dedicated transmission electron microscope (environmental transmission electron microscope, ETEM) with a differential pumping system [37, 60]. Gai et al. [61, 62] reported the pioneering work on the atomic resolution imaging in an ETEM. Normally, the gas introduced to the sample region is pumped separately from the rest of the TEM column. To confine the gaseous species, two or more pairs of extra apertures with small bores are installed in the objective pole pieces, as shown by the left panel in Fig. 2. Taking the commercial H-9500 ETEM from Hitachi company as an example, the gaseous environments can be achieved via gas injection from either the holder or the column. The former creates the gaseous atmosphere via the holder with a
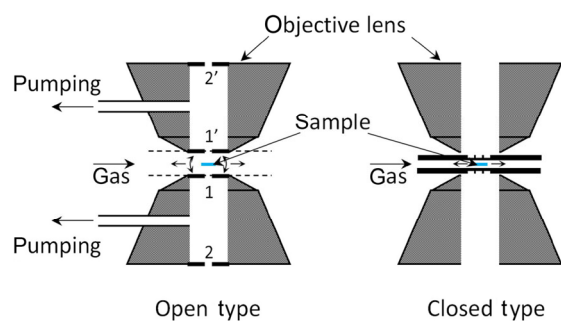
Figure 2 Conceptual schematics of the gas flow directions and adaptations for the open and closed types.

gas-introducing nozzle [63], and the gases are mainly local to the volume around the tip of the nozzle and thus the sample nearby. The latter builds a relative homogeneous pressure around the sample region and is applicable for all the holders (heating, cooling, biasing, mechanical loading, etc.) compatible with this ETEM.

Depending on the working principle of the open-type method, the pole pieces must be modified, or a new state-of-the-art ETEM must be acquired. The pressure in ETEM chamber is generally not higher than 20 mbar [64], with a gas path length of several millimeters (i.e., ~ 5 mm), as determined by the setup of the pole pieces and the apertures of the TEM. In the *in situ* experiments, the gas pressure is maintained by a continuous gas flow, which may break down the TEM vacuum system if a critical rise occurs. The low pressure compared with the atmospheric pressure can be beneficial for observing and measuring the dynamic and kinetic data accurately by reducing the growth or reaction rate. However, the phenomena and thermodynamic and kinetic data obtained from the low-pressure experiments may not be compatible to real situations where atmospheric or even higher pressures are necessitated for specific reactions.

2.2　Closed type

The closed-type method, which is also called the gas nanoreactor [65, 66], incorporates a gas flow and a heating system, along with a closed-window cell on a transmission electron microscope holder, as shown in Fig. 3. This method is widely applicable for liquid-involved experiments [67–70], which are beyond the scope of this review. A conceptual sketch of the
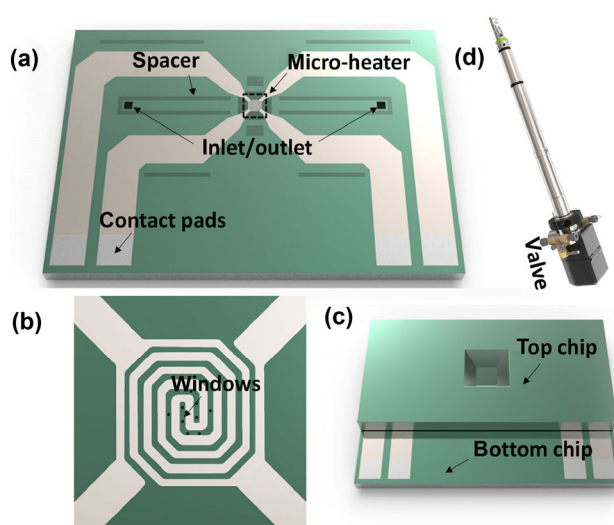

Figure 3 Schematic of bottom chip (a), spiral-shaped heater (b), and top/bottom chips (c) of the gas holder with a nanoreactor (d).

closed-type method is shown in Fig. 2 (right panel), indicating that the closed nanoreactor isolates the gas pressure inside from the outside. Furthermore, the nanoreactor comprises top and bottom chips separated by a rubber O ring (spacer), yielding a minimum height of approximately 3–4 μm for the cell [65, 71]. Electron transparent windows are preformed on the top and bottom chips (Fig. 3(b)), which can be aligned to overlap well and ensure high-resolution imaging. The window films must be thin, nonporous, strong enough to withstand the differential between the inner and outer pressures, and inert to the reactive gases. They must also have a low electron-scattering effect, such as the popular amorphous SiN_x and C films [72, 73]. A schematic of the gas holder from DENSsolutions company, which can achieve both static and flowing gaseous atmospheres by adjusting the valves, is shown in Fig. 3(d).

The functional holder is compatible with most of the standard TEMs without modifications. The gas pressure around the sample depends on the window films and can reach the atmospheric pressure with sub-nanometer or atomic-resolution [65, 74–76]. Currently, this is the only way to achieve the atmospheric pressure or higher [71, 77]. The design of the nano-reactor allows large-angle electron diffraction and high-angle annular dark-field (HAADF) imaging without the limitation of apertures [60]. However, the spatial resolution can be degraded by the double

window films with a thickness of 10–50 nm [65, 71, 73, 74, 78] and the gas layer between them, whose thickness depends on the nanoreactor design and gas pressure and is normally < 1 mm [65, 71, 72, 74, 79, 80]. Moreover, it is complicated and difficult to achieve the good alignment of the windows on the bottom and top chips. Additionally, the window films may be damaged by intense electron beam during *in situ* observations, causing the experiments to be aborted. Table 1 summarizes the major differences between the open and closed-type methods.

2.3 Other approaches

In addition to the aforementioned two typical methods for creating a gaseous atmosphere inside a transmission electron microscope, other approaches have been used successfully. McDonald [81] and Hammar [82] reported a modified ultrahigh vacuum (UHV) transmission electron microscope with a base pressure of 10^{-9}–10^{-10} Torr (vacuum of 10^{-6}–10^{-7} Torr in regular TEMs), which was combined with gas-feeding systems. In this method, excellent clean conditions are first established, and then controlled-atmosphere environments are established with low pressures. Currently, the UHV transmission electron microscope is widely adopted in the study of nanomaterial growth and facilitates the measurement of kinetics owing to the slow nucleation and growth processes under low-pressure conditions. In addition to setting up gas-introduction systems, researchers have attained gaseous environments via the evaporation of solid materials [83–85]. However, the pressures are not easily controllable.

3 Observing NW growth

One popular research area that benefited from the development of controlled-atmosphere TEM techniques is the *in situ* growth of NWs, such as semiconductor and metal-oxide NWs, which have great potential in electronics and energy applications. In this section, we describe recent progress in the understanding of growth mechanisms, dynamics, and kinetics, as well as novel nanostructure designs on such an *in situ* platform.

3.1 Growth mechanisms

The mechanisms of NW growth from vapor can be summarized as catalytic growth (vapor–liquid–solid (VLS) and vapor–solid–solid (VSS)) and catalyst-free growth. Since it was proposed by Wagner et al. [86] in 1964, the VLS mechanism has attracted extensive attention. NW growth by this mechanism involves vapor, liquid, and solid phases, with the characteristic feature of a liquid eutectic mediating the mass transport from the vapor to the solid interface. Yang et al. first demonstrated *in situ* the validity of the VLS mechanism in TEM at the nanoscale in Ge and GaN NW growth [83, 84]. The ever-increasing efforts towards real-time observations have greatly elucidated the VLS mechanism [47].

The VLS mechanism can be divided into three stages—(I) alloying, (II) nucleation, and (III) growth—as shown in Fig. 4 [83]. Kim et al. [87] systematically studied the first stage during Si NW growth that starts with solid Au catalysts. They found when the Si atoms incorporate into the solid Au cluster, a liquid

Table 1 Major differences between the open and closed-type methods

|	Open type	Closed type
Construction	Differential pumping system and apertures	Nanoreactor
Compatibility	Any type of holders	Standard TEMs
TEM modification	Yes	No
Working mode	Flow	Static and flow
Electron scattering	Gas layer	Window films and gas layer
Thickness of gas layer	The order of millimeters (i.e., ~ 5 mm), decided by the pole pieces and apertures	< 1 mm, decided by the spacer thickness and gas pressure
Maximum pressure	Normally < 20 mbar	1 bar or higher
Possible breakdown reason	Problems in pumping system and apertures	Rupture of windows
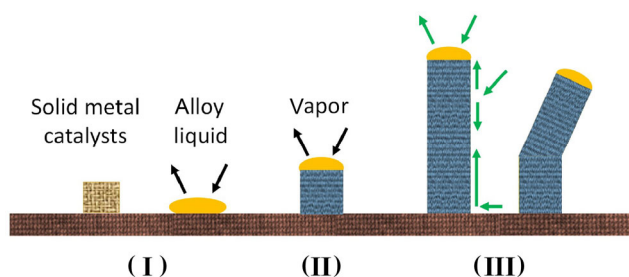
Figure 4 Simplified processes in the VLS mechanism: alloying (I), nucleation (II), and growth (III). The black arrows indicate the atoms moving into and out of the droplet, and the green arrows in stage (III) indicate pathways of the atoms added during the NW growth. Adapted with the permission from Ref. [83], © American Chemical Society 2001.

AuSi phase emerges at the surface, forming a mixed phase of Au and AuSi; then, the interface propagates nonlinearly towards the side of the pure Au phase. After shrinking to a critical size, the Au cluster disappears rapidly, forming a single-phase AuSi droplet. The continuous dissolution of Si into the AuSi droplet leads the growth to the second stage, i.e., nucleation, which occurs suddenly at the droplet edge [88]. Critical supersaturation is needed to start the nucleation process, but once the solid nucleus forms, growth on the existing nucleus requires less supersaturation.

The NW growth proceeds with additional atoms condensing at the solid–liquid interface, resulting either from direct impingement or diffusion on the side wall and substrate surface [89], as indicated by the green arrows in stage (III) in Fig. 4. Ross et al. [90–92] studied the effects of the catalyst during the NW growth. When grown at low pressures (i.e., 10^{-8}–10^{-5} Torr) and high temperatures (i.e., 500–650 °C), the NWs exhibited an oscillatory sawtooth-faceted morphology. Au decoration on the sidewalls and surface-energy contributions of the droplet, facet, and interface with different NW diameters are believed to account for the formation of such a periodic shape. Au also exhibits a strong propensity for Ostwald ripening during growth at 600 °C, e.g., migrating from the small droplets to the large ones via the sidewalls, which can cause the widening or narrowing of the NW with the growth time. Such Au migration can be relieved by higher pressures, contaminants from the precursor, and a small amount of O_2 but are aggravated

by higher temperatures. In addition to axial growth, numerous nanostructures—such as the kinking structure shown in Fig. 4 (III)—have been grown by adjusting the growth parameters and thus the thermodynamic and kinetic conditions to introduce a new facet [93]. The design of complicated nanostructures will be discussed in detail later.

In addition to the classical Si NWs, the VLS mechanism was also observed in the growth of Ge [94, 95], GaN [96, 97], GaP [98, 99], and InAs [100]. Surprisingly, during Au-catalyzed Ge NW growth, the liquid droplet persisted below the eutectic temperature, as demonstrated by the smooth round shape of the catalyst in Fig. 5(a). At the same Ge_2H_6 pressure and temperature, the Ge NWs grew with a solid catalyst as well (demonstrated by the faceted surface in Fig. 5(b)), at a slower growth rate than that for the VLS growth. The robust VLS growth under the eutectic temperature was not a consequence of the Gibbs–Thomson effect or the size effect but resulted from the growth history: A high Ge supersaturation in the droplet inhibits the nucleation of the solid clusters [94]. When the growth temperature is reduced far below the eutectic temperature, the catalyst is definitely solidified, and the NWs grow via the VSS mechanism. Currently, Pd [101], $AlAu_2$ [102], Cu [103], and AuAg [104, 105] have been demonstrated as effective solid catalysts for growing Si/Ge NWs.

Although attention has mainly been paid to VLS and VSS growth assisted by catalysts, catalyst-free growth commonly occurs, especially for metal-oxide NWs grown in the presence of O_2 [106–108]. One
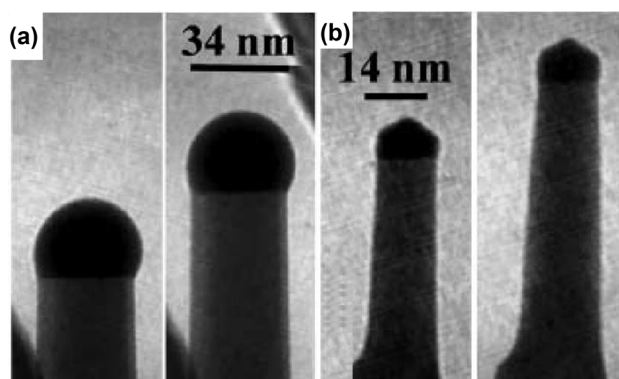

Figure 5 Ge NW growth via the VLS (a) and VSS (b) mechanisms with respect to time. Reproduced with permission from Ref. [94], © The American Association for the Advancement of Science 2007.

widely accepted mechanism is vapor–solid (VS) growth, in which vapor sources condense directly on the substrate to nucleate and grow into a one-dimensional structure, driven by the crystal anisotropy and defects or assisted by O_2. Recently, we reported the growth of $W_{18}O_{49}$ NWs via the VS mechanism by the thermal oxidation of tungsten. Autocorrelation analysis revealed that in contrast to the case of VLS, adjacent nucleation events in this VS growth are independent. There is another possible mechanism—solid diffusion—wherein NW growth is accomplished via the incorporation of O from vapor and metal ions through diffusion along the defects, such as twin boundaries, stacking faults, or surfaces, from the substrate to the NW tip. Rackauskas et al. [109] performed direct CuO NW growth thermally oxidizing metallic Cu. Figures 6(a) and 6(f) show schematics of the CuO growth corresponding to the growth in Figs. 6(b)–6(e) and Figs. 6(g)–6(l), observed from the directions parallel and perpendicular to the twin boundary, respectively. The atom layer nucleates at the edge of the twin boundary ridges, with a layer thickness of 0.23 nm (Figs. 6(b) and 6(g)), indicating the atomic layer-by-layer growth of the (111) planes. After the nucleation, the step advances from one side to the other, as indicated by the white arrows in Figs. 6(b)–6(e) and 6(g)–6(l). After comparing the incubation time for nucleation and the lateral and ridge growth time, the authors suggested that the NW growth is limited by the nucleation of a new layer rather than the diffusion of Cu ions along the twin boundary from the substrate to the NW tip.

3.2 Growth dynamics and kinetics

In situ observations of the NW growth dynamics allow the derivation of quantitative information regarding the growth rates, rate-limiting steps, kinetics, and activation energies for various processes, which is difficult to attain via other techniques. According to the Gibbs–Thomson effect, the growth rate increases with larger diameters. However, Kodambaka et al. [110] measured the Au-catalyzed VLS growth of Si NWs *in situ* and reported that the growth rate was independent of the NW diameter, proportional to the pressure of Si_2H_6, and inversely proportional to the temperature. The Si removal, relative to the chemical potential, is considered to be irrelevant to the growth rate, and the rate only depends on the dissociative adsorption of Si_2H_6. Regarding VSS growth, Hofmann et al. [101] studied the dependence of the growth rate in Pd-catalyzed Si growth on the interfacial reaction and diffusion and proposed that the growth is controlled by the outward diffusion of Pd and the inward diffusion of Si. Kim et al. [88] identified the activation energies for the dissociative adsorption of Si_2H_6 and
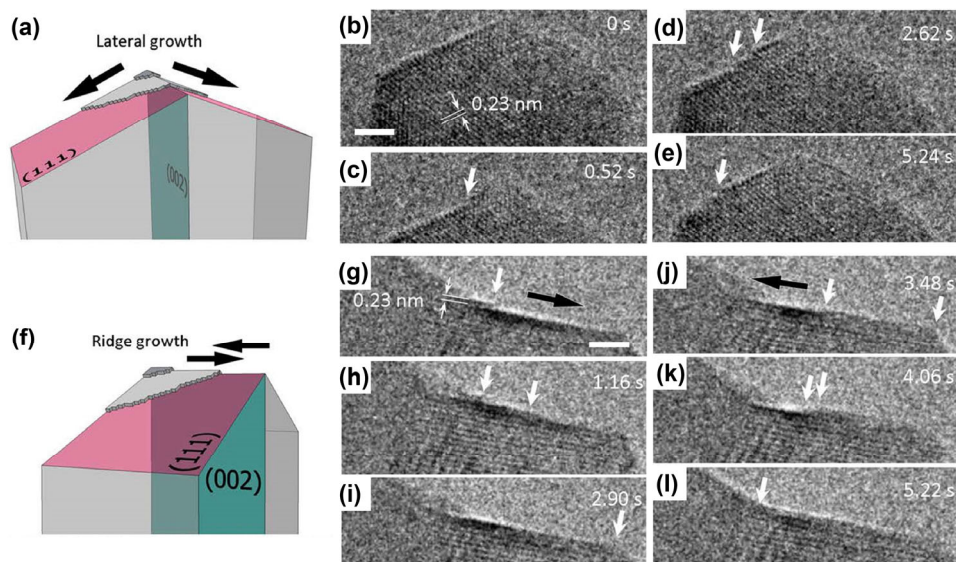

Figure 6 Growth of CuO NWs observed from the directions parallel (a) and perpendicular (f) to the twin boundary. Step advancing from the tip and sideways (b)–(e), from left to right (g)–(i), and from right to left (j)–(l). The scale bar represents 2 nm. Reproduced with permission from Ref. [109], © American Chemical Society 2014.

Si incorporation from a AuSi liquid into a Si crystal according to the vapor–liquid and liquid–solid rate constants by quantifying the Si growth.

In addition to the unique advantage of extracting the growth-rate information, *in situ* TEM facilitates the study of the kinetics of the step flow and the oscillatory behavior. Real-time observations [101–103] indicated that step flow at the NW/catalyst interface plays a significant role in the NW growth. Wen et al. [102] reported a fast step-flow process in Si NW growth with a liquid AuSi droplet, as shown in Fig. 7(a), such that the addition of a new layer was impossible to measure. However, for VSS growth, the steps flowed more slowly, and the propagation across the interface (Fig. 7(b)) could be monitored. They further studied the different step kinetics in VSS and VLS growth [111] and demonstrated that the second derivative of the free energy per unit volume evaluated at the equilibrium composition is the most important parameter related to the kinetics, which reflects the size, ease of step nucleation, and alloy thermodynamics of the growth system.

Oscillatory behavior has been widely observed in VLS and VSS growth. When the NW sidewall facets are not parallel to the growth axis, surface oscillations may occur and trigger facet alternation [90]. Droplet oscillation is also normal [103, 112, 113], such as jumping from one facet to another because of a mismatch between the catalyst size and the wire diameter or pinning/unpinning from the trijunction. Another kind of the oscillatory behavior is mass transport from the growth interface [114, 115]. Gamalski et al. [115] reported the Au-catalyzed growth of Ge NWs,

accompanied by the cyclic oscillation of the truncated edge at the trijunction. Similar nonplanar interfaces were reported in the Au-catalyzed growth of GaP [99], the self-catalytic VLS growth of Al_2O_3 [114], and the catalyst-free VS growth of $W_{18}O_{49}$ [116].

We grew $W_{18}O_{49}$ NWs/nanotubes *in situ* in the absence of catalysts via the thermal oxidation of a tungsten filament at a pressure of 0.1 Pa O_2 and 700 °C within an ETEM [116, 117]. Figures 8(a)–8(e) shows the characteristic feature of the NW growth: oscillatory mass transport on the NW tip. The $W_{18}O_{49}$ NW grows along the [010] direction (schematic in Fig. 8(f)), and the thickness of the additional layer is 0.38 nm, as shown in Fig. 8(e), indicating the monolayer growth of the (010) planes. The curves of the truncated area and added monolayers are plotted with respect to time in Figs. 8(g)–8(h), demonstrating that cyclic oscillation occurs with the NW growth. The growth cycle starts with the atoms filling the truncated tip rim (right); then, solid nucleates on the terminal facet, followed by mass transport from the tip rim to the newly formed step. This results in the growth of a new layer, yielding a truncated tip rim again, which completes the cycle. All the step-flows were quantified with approximately the same growth rate, which is far higher than that for filling the truncated corner. Therefore, the atom filling in the truncated corner is the rate-limiting step for the growth of $W_{18}O_{49}$ NWs.

The nonplanar trijunction in VLS and VSS growth is attributed to the balance of the facet energy and the droplet surface tension, and the periodic morphology change of the trijunction may arise from the time-varying chemical potential of the catalysts, i.e., the
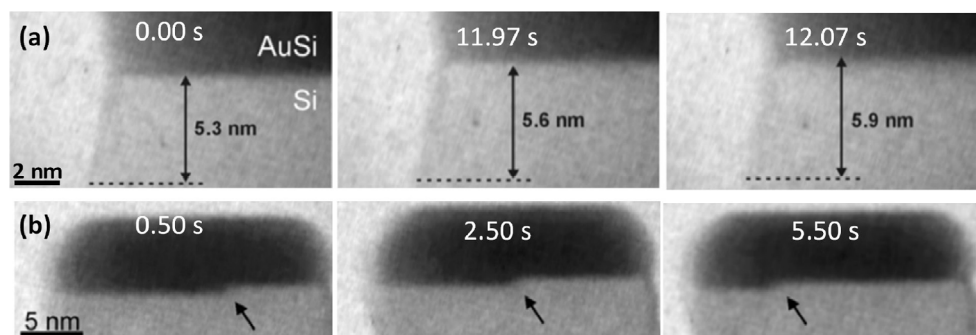

Figure 7 Step flow during Si NW growth with a liquid AuSi droplet (a) and a solid AlAu$_2$ catalyst (b). Reproduced with permission from Ref. [102], © The American Association for the Advancement of Science 2009.
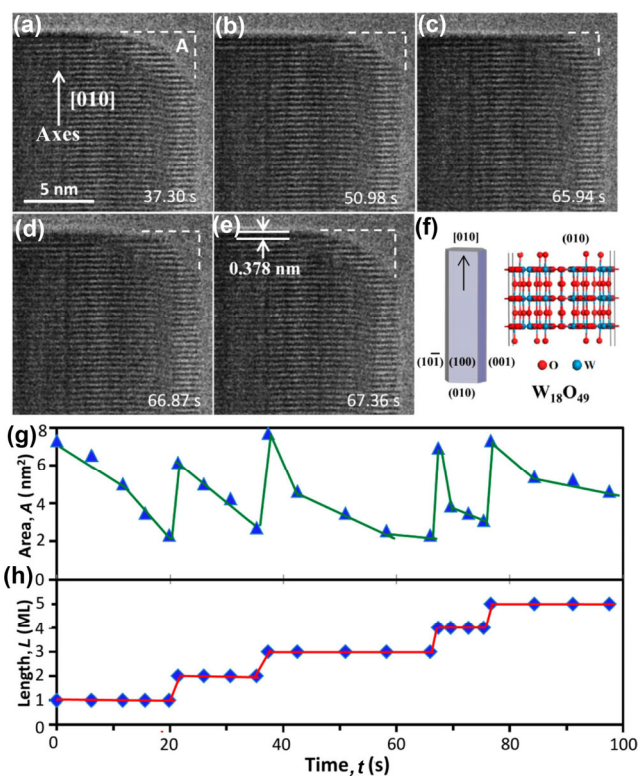
Figure 8 Oscillatory mass transport during NW growth (a)–(e). (f) Schematic of the $W_{18}O_{49}$ NW. (g) and (h) Time-dependent truncated area and added monolayers. Reproduced with permission from Ref. [116], © American Chemical Society 2016.

catalyst composition [99, 114, 118]. In catalyst-free VS growth, the role of the catalysts is replaced by vapor supplied with a steady pressure, and the shape oscillation of the NW tip rim (from truncated to nearly rectangular and back to truncated) reflects the energy balance of the NWs. In slow growth, the rough tip rim (corner) of the NWs is filled first, as it is energetically favorable for vapor deposition. Tersoff et al. first proposed the growth model [119] and suggested that when the energy increase of the atoms added to the corner is larger than that of the nucleation on the terminal facets, the growth of the corner is interrupted by additional atoms nucleating on the terminal facet. Then, the atoms at the corner move the edge of the nuclei on the terrace, decreasing the total surface energy.

Oscillatory behavior is not limited to the growth process; it was also observed in the reshaping process of MoO_2 NWs under electron-beam irradiation and heating at 600 °C in 0.05 Pa O_2 [120]. The reshaping process comprises the dissolution of the tip facets and growth along the sidewall. The dissolved species on the tip migrate to the sidewall via surface diffusion, because of the electron beam-induced O-loss on the tip surfaces. When examining the dissolution of the tip facets, we observed a cyclic oscillatory behavior, as shown in Fig. 9. The dissolution starts at the edge site, as indicated by the red arrows in Figs. 9(a)-I. Subsequently, the dissolved step propagates towards the middle region until the outmost layer vanishes and the subsurface layer is exposed, revealing a flat tip surface and leading to the shortening the NWs (I–IV). A schematic of the corresponding oscillatory behavior is presented in Fig. 9(b).

3.3 Designing novel nanostructures

On the basis of the understanding of the growth
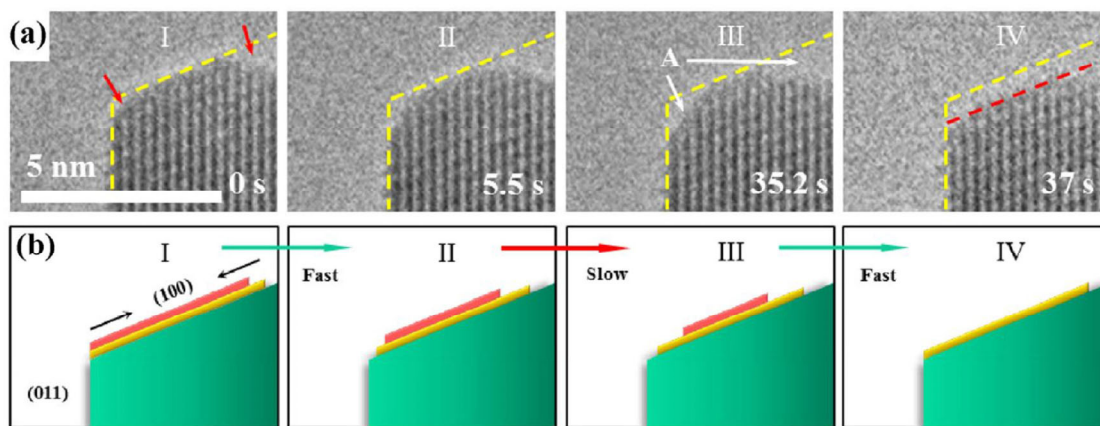

Figure 9 Oscillatory dissolution of the tip facet of a MoO_2 NW (a) and (b). The surface and subsurface layers are indicated by red and yellow lines, respectively. Reproduced with permission from Ref. [120], © Springer 2016.

mechanisms and the relationship between the kinetics and growth conditions, many complicated nano-structures have been designed, such as the single NW with different diameters and growth directions [91, 100, 121, 122]. Examining the droplet geometry, which is exemplified by the volume and the contact angle, revealed that the diameter change in steady-state growth highly depends on the catalyst particle, the precursor, and the temperature. Growth-direction change, i.e., kinking from one direction to another, can be achieved via perturbations in the local environment and kinetic control. Schwarz et al. [93, 112, 123] systematically studied NW growth with various morphologies and proposed that the interfacial energy on the sidewall, edge cost, and droplet jumping play significant roles in the growth modes, which could be perturbed by the temperature, asymmetric incidence of precursors, and other growth parameters in the experiments.

The growth of heterostructures [104, 122, 124] has also attracted considerable interest, as they potentially have interesting functions compared with their coun-terparts, such as Si/Ge, InP/GaP, Si/GaP, GaP/Si, and GaAs/Ge. Recently, Panciera et al. [125] embedded a faceted metal silicide nanocrystal (NC) inside Si NWs via sequential catalyst reactions. The NiSi initially forms in the liquid droplet and finally incorporates endotaxially to form a metal silicide/Si heterostructures.

The properties of III-V semiconductor NWs can be tailored by controlling the wurtzite (WZ) and zincblende (ZB) phases in isomer structures [126–128], although the ZB phase is thermodynamically stable for the bulk material. Numerous factors—including the supersaturation, diameter, interfacial energy, and chemical potentials—have been proposed to elucidate the mechanisms of phase formation [126, 129, 130]. Recently, Jacobsson et al. [131] observed the phase switching in GaAs NWs *in situ*, as shown in Figs. 10(a)–10(c), which show the interface dynamic and droplet volume changes that occurred during the controllable growth. The WZ growth proceeded via the step flow across the interface and was proportional to the AsH$_3$ pressure, demonstrating that the growth rate was limited by the incorporation of As. During the ZB growth, the step flow became too fast to observe
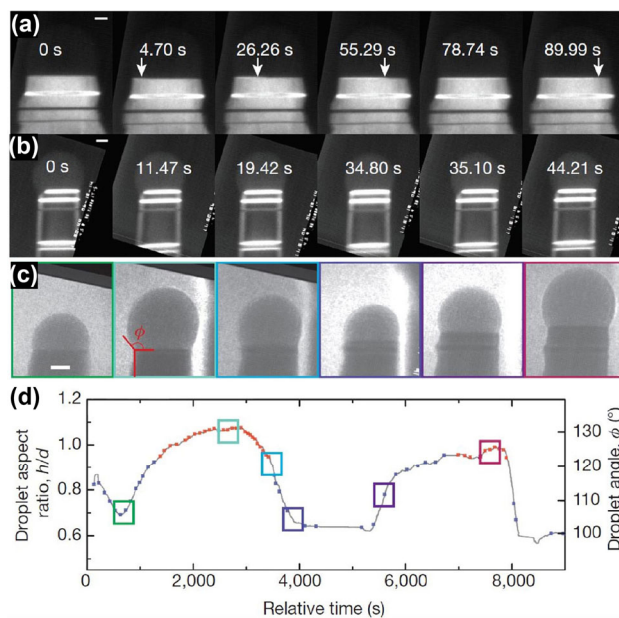

Figure 10 *In situ* growth of GaAs NWs with WZ (a) and ZB (b) crystalline structures. (c) and (d) Droplet evolution during the WZ-ZB growth of GaAs. Reproduced with permission from Ref. [131], © Nature Publishing Group 2016.

(Fig. 10(b)), and the droplet exhibited oscillatory behavior. Furthermore, the crystalline structure was controlled by adjusting the As/Ga ratios by changing the pressure of the AsH$_3$ precursor, yielding WZ at a high As/Ga ratio and ZB at a low ratio. However, the structure was not directly determined by the AsH$_3$ pressure according to the delayed response but rather by the droplet geometry. The phase switching occurs at the critical size of the droplet, i.e., height/diameter = 0.95, as shown in Fig. 10(d).

4 Observing catalysts at work

Another intensively studied area related to controlled-atmosphere TEM techniques is heterogeneous catalysis. Undoubtedly, TEM plays an irreplaceable role in visualizing the atoms in the catalysts. Numerous review articles have been reported to summarize this prevalent application [132–138]. Over 90% of the commercial chemicals in the industry are catalytically produced at manufacturing stages [139], mostly via gas-involved processes. Therefore, we focus on the catalyst behavior in gaseous environments, including sintering, surface, shape, and composition changes and the effects of these changes on the reactivity.

4.1 Sintering

Sintering is one typical phenomenon accounting for catalyst deactivation. The influence of external stimuli on the catalyst movement and sintering has long been studied using transmission electron microscopes [140–143]. According to the Thompson–Freundlich equation, Ostwald ripening drives the large particles to be larger at the cost of the loss of the smaller ones, owing to the lower chemical potential of the larger crystals. Simonsen et al. [144, 145] recorded the sintering of Pt NCs on the substrates of Al_2O_3 and SiO_2 *in situ* in air at a pressure of 10 mbar and 650 ℃, mediated by Ostwald ripening. However, NC loss was not observed in N_2 environments, indicating the indispensable effects of O_2. Some volatile Pt–O species may form and lead to the shrinkage of Pt NCs. A similar phenomenon [146] was observed in H_2-induced Ostwald ripening in Pd/Au systems, where H reduced the binding energy of the atoms, leading to the decomposition of the clusters.

4.2 Surface structure changing

The surface of the heterogeneous catalyst is the center at which reactions occur, as the catalyst adsorbs one or more reactants and catalyzes them to react at the active sites. Tremendous efforts have been directed towards designing various surface terminations and retrieving atomic-resolution structural information [147–151]. However, the stability of the predefined surface termination is not always straightforward [152–156]. Relaxation, reconstruction, and cover layers occur extensively, especially under external stimuli such as gaseous species and heating. Yoshida et al. [157] reported the surface relaxation of Au NCs supported on a CeO_2 substrate during CO oxidation inside an aberration-corrected ETEM. As shown in Fig. 11, the Au surface structure in vacuum differs from that in the CO/air environment at a total pressure of 45 Pa and room temperature. The lattice spacing (0.20 nm) of the Au NCs in vacuum well corresponds to that of the (200) planes in bulk Au. However, for the CO/air mixture, the atom columns near the surface shift and the lattice spacing changes to 0.25 nm, leading to a different surface structure (Fig. 11(b)). In light of the explicit calculations, the authors proposed that such a surface structure promotes the adsorption of CO molecules on the Au surface and sustains a high coverage of CO owing to the unusual bonding configuration with the second topmost surface layer.

Reconstruction with a different two-dimensional structure is another common phenomenon in surface
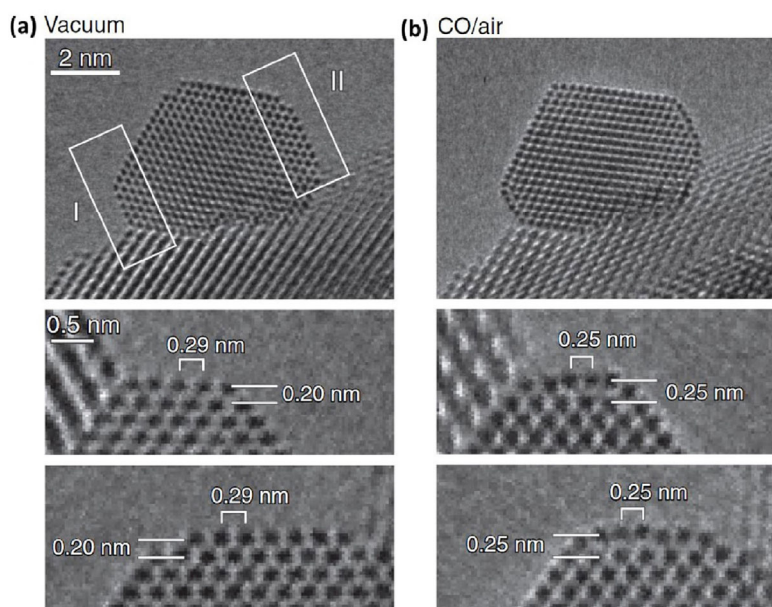

Figure 11 Au surface structures in vacuum (a) and 1 vol% CO in an air environment (b). Reproduced with permission from Ref. [157], © The American Association for the Advancement of Science 2012.

changing [158, 159]. We recently reported a {100}-(2 × 2) surface reconstruction for Pt nanocatalysts [160]. Figure 12 shows the surface reconstruction from side and top views when the Pt NCs were heated at an O_2 pressure of 0.1 Pa and 400 °C in an ETEM. The O_2 first reacted with the surface graphene layers and eliminated the graphene on the Pt NCs, as shown in Figs. 12(a)–12(d). Then, promontories appeared on the clean Pt surfaces, such as (010), (001), and even high-index facets (marked in Fig. 12(e)). The distance between the adjacent promontories on the (001) facet was 0.39 nm, which is twice the interplanar distance of the (002) planes in bulk Pt, indicating a 2× super-structure. The top-view TEM images in Figs. 12(f) and 12(g) indicate interplanar distances of 0.56 and 0.54 nm, which are approximately twice the normal spacing of the (110) planes. By combining the side and top-view observations, we confirmed the formation of a Pt-{100}-(2 × 2) reconstruction. The structure based on the O-adsorption model is presented in Fig. 12(h), for which the simulated TEM images are well-consistent with the experimental results.

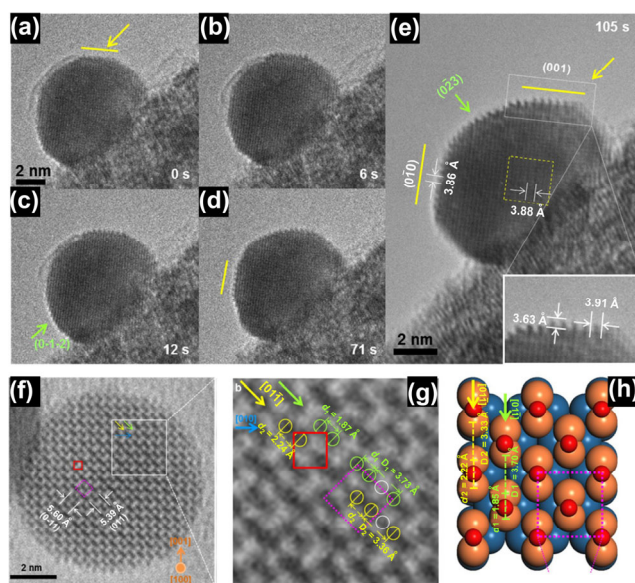A similar (1 × 4) reconstruction was observed on the (001) surface of the anatase TiO_2, which is normally known as a high-energy surface in the anatase bulk phase. Within an ETEM, we revealed the dynamic formation of a (1 × 4) reconstruction under the protection of O_2, as shown in Figs. 13(a)–13(d) [161]. The anatase was initially covered by an amorphous layer (Fig. 13(a)), which was almost completely removed at 34.9 s (Fig. 13(b)). Simultaneously, a crystalline TiO_x layer formed on the (001) surface (Fig. 13(c)) and tended to align regularly. Finally, the adsorbed layer evolved into the stable 4× periodicity structure (Fig. 13(d)). The TEM images and line profiles of the intensity (Figs. 13(e) and 13(f)) support the result that the surface reconstruction proceeded via the removal of amorphous organics and the alignment of the residual TiO_x species.

Further *in situ* investigation of the early stages of the reconstruction process is shown in Fig. 14, demonstrating the formation of intermediate metastable configurations, e.g., 3d/5d structures ("d" indicating the normal periodicity), prior to the final (1 × 4) reconstruction. Figure 14(a) shows the evolution from 3d-3d-4d to 4d-4d-3d and finally to 4d-4d-4d, and the stable and unstable states are statistically depicted in Fig. 14(b). According to the *in situ* experimental results, we proposed that the (1 × 4) reconstruction on the (001) surface forms via the following process: (1) TiO_x species first attach to the surface randomly; (2) TiO_x species aggregate into islands or small rows; (3) metastable 3d, 4d, and 5d structures form; (4) the metastable structures partially transform into a 4d pattern; and (5) a (1 × 4) reconstruction finally forms. The first three steps are dominated by the tendency to reduce the number of dangling bonds, and the subsequent steps are driven by the surface stress.

In addition to the relaxation and reconstruction, the surface also changes with the formation of cover layers, such as graphene layers [160, 162]. Recently, Zhang et al. [163] reported the formation of an amorphous layer on the surface of TiO_2 in a gaseous environment similar to that used for water-splitting reactions. The anatase NCs were synthesized mainly with smooth {101} surfaces, as shown in Fig. 15(a). When exposed to water vapor at 1 Torr and an electron beam at 150 °C, the initial crystalline surface of titania was covered by a thin disordered layer,

Figure 12 Side (a)–(e) and top-view (f) and (g) TEM images obtained during the formation of a Pt-{100}-(2 × 2) reconstruction. (h) Structure based on the O-adsorption model. Orange and blue represent the surface and bulk Pt, respectively, and the red balls represent O. Reproduced with permission from Ref. [160], © Chinese Materials Research Society 2016.
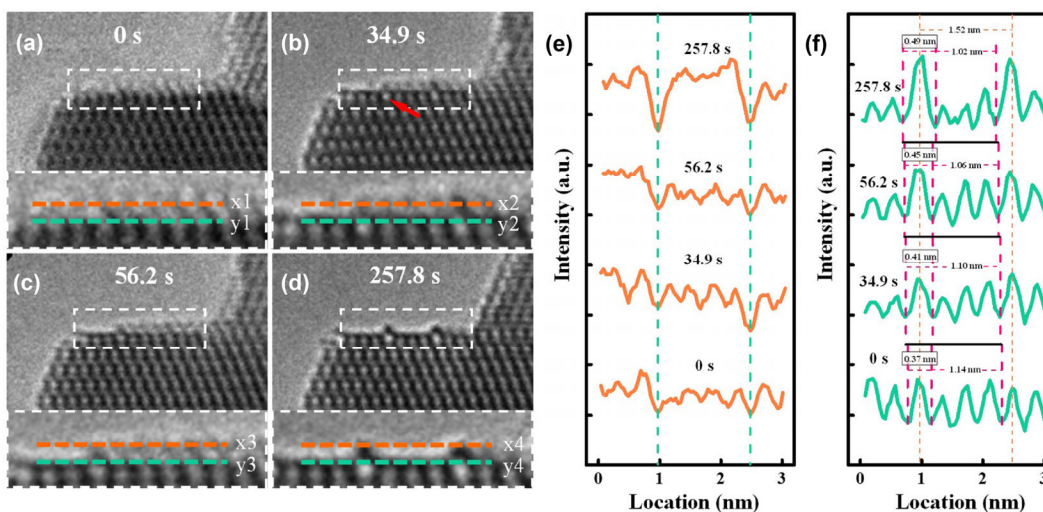
Figure 13 TEM images (a)–(d) and line profiles of the intensity (e) and (f) during the reconstruction formation. The orange and green lines indicate the reconstructed layer and top-surface layer, respectively. Reproduced with permission from Ref. [161], © American Chemical Society 2016.
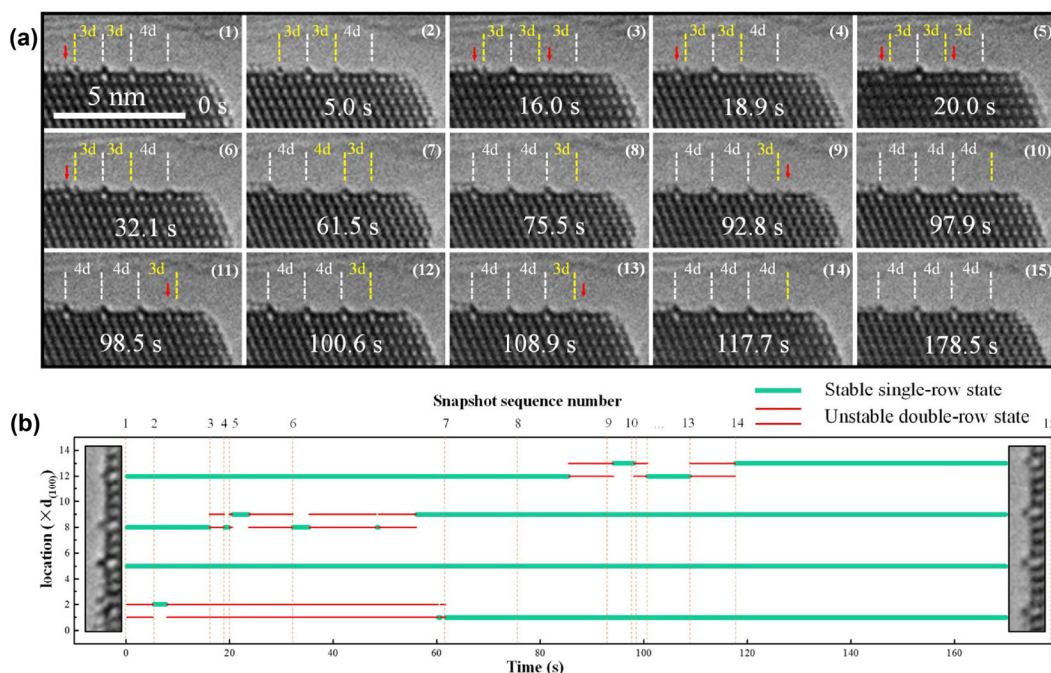

Figure 14 Atomic evolution (a) and a statistical diagram of the TiO$_x$ locations (b) during the formation of the (1 × 4) reconstruction. Reproduced with permission from Ref. [161], © American Chemical Society 2016.

which was slightly thickened over time (Figs. 15(b)–15(e)). An amorphous layer was also present under the water exposure and light irradiation but was absent in a H$_2$ atmosphere or without the electron beam, as shown in Fig. 15(f). Combining all the experimental results, the authors demonstrated the significant roles of an electron beam/light and water vapor in the surface amorphization. Further analysis indicated that the disordered layer is hydroxylated titania with +3 titanium and revealed a Ti^{4+} reducing process that occurs during the photocatalytic splitting of water.

4.3 Shape changing

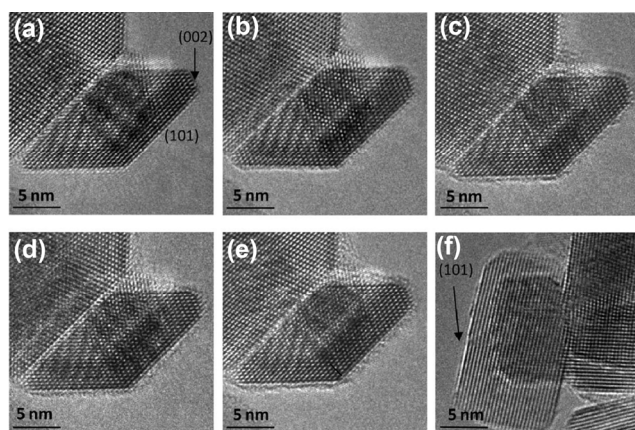Many studies [164–166] have shown that the shape of

Figure 15 Anatase particles at 150 °C under various conditions: (a) no water, (b) 1 h of exposure to water, (c) 7 h of exposure to water, (d) 20 h of exposure to water, (e) 40 h of exposure to water; (f) fresh surface without electron-beam irradiation after 40 h in water gas. The water pressure is 1 Torr. Reproduced with permission from Ref. [163], © American Chemical Society 2013.

Figure 16 TEM images (a)–(c) and corresponding FFT patterns (d)–(f) obtained during the morphology evolution of the PdCu NC. The scale bar represents 10 nm. Reproduced with permission from Ref. [169], © John Wiley and Sons 2016.

heterogeneous catalysts responds far more dynamically to the change of gaseous environments than previously anticipated. By using an ETEM, Hansen et al. [167] obtained the dynamic shape responses of Cu NCs supported on a ZnO substrate to H_2, CO, and H_2O (and a mixture thereof). When exposed to a mixture of H_2O and H_2, the Cu NCs tended to transform into a round shape with an increasing fraction of (100) and (110), owing to the H_2O-adsorption-induced change of the surface energy. In a mixed atmosphere of CO and H_2, they were transformed into a more disc-like shape with a reduced interface energy. A similar phenomenon was observed for Au NCs supported on CeO_2, according to Uchiyama et al. [168]; i.e., Au NCs remained faceted in CO-rich gas but transformed into a round shape in a pure O_2 atmosphere.

We recently investigated the behavior of bimetallic PdCu NCs at an atmospheric pressure of H_2 and investigated the effect of the pressure on the morphology of PdCu NCs [169]. The as-synthesized spherical PdCu NCs with a primitive cubic (B2) crystalline structure (indicated by the lattice spacing in Fig. 16(a) and fast Fourier transform (FFT) pattern in Fig. 16(d)) were annealed in 1 bar H_2 at 600 K. It was discovered that the PdCu NC transforms into a truncated cube over time, as shown in Figs. 16(a)–16(c). The atomically resolved HAADF images (inset in Fig. 17) indicate no segregation in the NCs or on the
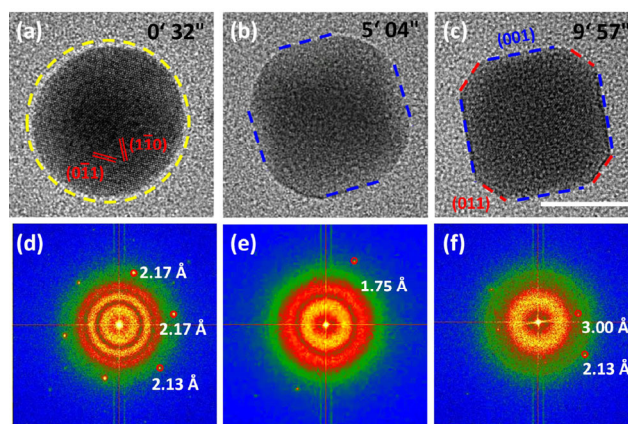
surface before and after the transformation. Intriguingly, such a transformation was not observed at low H_2 pressures, such as 0.016 bar.

As previously discussed, the adsorption-induced change of the surface energy may account for the NC reshaping in equilibrium [165, 167, 168, 170]. One typical method for calculating the corrected surface energy is to use the following equation

$$\gamma_{hki}^{int} = \gamma_{hkl} + \theta \frac{E_{ads}}{A_{at}} \tag{1}$$

where γ_{hkl} is the (hkl) surface energy per unit area, E_{ads} is the adsorption energy, A_{at} is the surface area per surface atom, and θ is the surface coverage. θ can be determined using Eq. (2), where p is the gas pressure, and K is the Langmuir isotherm constant, which contains the temperature and adsorption energy terms.

$$\theta = \frac{pK}{1 + pK} \tag{2}$$

After the corrected surface energies are determined, a basic understanding can be obtained via the Wulff construction, which is based on the following equation

$$\frac{\gamma_{hkl}}{d_{hkl}} = \text{constant} \tag{3}$$

where γ_{hkl} is the surface energy, and d_{hkl} is the distance from (hkl) to the center.
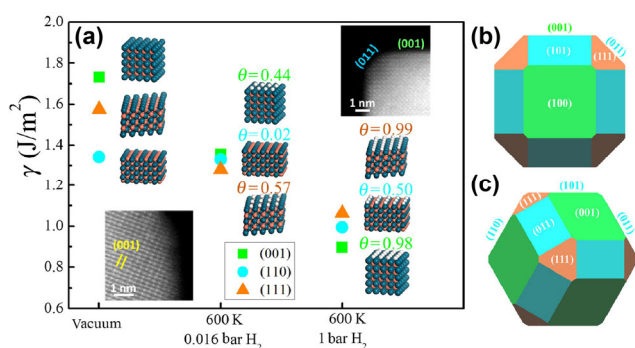
Figure 17 Surface energies of the (001), (110), and (111) surfaces at different pressures (a). Blue, orange, and white represent Pd, Cu, and H, respectively. (b) and (c) Wulff constructions of the PdCu NCs projected from the [100] and [111] directions, respectively. Reproduced with permission from Ref. [169], © John Wiley and Sons 2016.

By combining first-principles calculations with this method, the corrected surface energies under different H_2 pressures were derived, as shown in Fig. 17. The energies for the (001), (110), and (111) surfaces vary with respect to the H pressures. At 0.016 bar, the surface energies are similar; hence, the PdCu NCs exhibit a round shape. However, when the PdCu NCs are exposed to 1 bar H_2, the (001) surface exhibits a far smaller energy than the other two surfaces. The Wulff constructions for the H-terminated PdCu NCs with the corrected surface energies are shown in Figs. 17(b) and 17(c), which are perfectly consistent with the experiments for both the [100] and [111] directions, respectively.

In addition to the gas adsorption-induced shape change, other factors should be noted, such as the change of the interfacial energy and the formation of hydrides or oxides. Zhang et al. [171] reported a shape change of Pd NCs induced by the formation of overlayers from a reducible TiO_2 substrate due to the strong metal–support interaction. In a reducing atmosphere, an amorphous TiO_x layer wrapped Pd NCs, and crystallized at 500 °C. As shown in Fig. 18, the Pd NCs originally exhibited a round shape with a truncated corner (Fig. 18(a)). However, when the crystalline layer formed, the (111) facets expanded, and other facets shrank or fully vanished, resulting in a faceted shape (Fig. 18(f)). The shape-changing process from Fig. 18(a) to Fig. 18(f) is summarized by the schematic in Fig. 18(g). Considering the surface energy, the authors suggested that the TiO_x layer can increase the surface-energy ratio of the (100) surface (and other high-energy surfaces) to the (111) surface and hence increase the area of the (111) surface.

4.4 Composition changing

Considering the element distribution in bimetallic or multicomponent NCs, attention should be paid to the composition change in gaseous environments [146, 172–176]. Xin et al. [177] reported that PtCo NCs exhibit significantly different element distributions in O_2 and H_2 atmospheres. CoO islands formed during annealing in the O_2 environment, whereas these were reduced by H_2 and Co migrated back into the bulk, leaving a Pt layer on the surface. Wu et al. [178] explored the chemical evolution during the reduction and oxidation of Ag/AgCl heterogeneous nanostructures. They employed an electron beam as a reducing
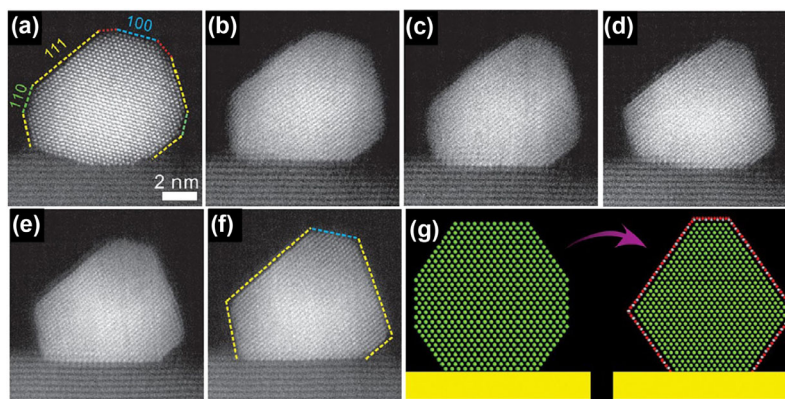

Figure 18 HAADF images (a)–(f) and schematic (g) of the shape change of a single Pd NC on TiO_2 during overlayer formation. Green, red, and gray represent Pd, O, and Ti, respectively. Reproduced with permission from Ref. [171], © American Chemical Society 2016.

agent in the reduction process, which was suggested to result from the removal of Cl and the trapping of electrons to Ag$^+$. When heated at the atmospheric pressure and 200 °C, the Ag/AgCl heterostructures were oxidized, which can be divided into two steps. The TEM images in Figs. 19(a)–19(d) show the considerable change that occurred during the oxidation process. The selected-area electron diffraction (SAED) pattern in Fig. 19(e) shows the composition of the Ag/AgCl heterostructures, which were oxidized to Ag first, as indicated by the diffraction spots in Fig. 19(f).

The second step is the oxidation of Ag to AgO, as indicated by the spots in Figs. 19(g) and 19(h).

4.5 Influence on reactivity

The aforementioned changes of the catalysts significantly affect their catalytic behaviors by altering the area, facets, and configurations of the surface, which are strongly related to the active sites and the number thereof [179–181]. We recently studied the dependence of the velocity of graphene oxidation on the facets of catalysts *in situ* [162], as shown in Fig. 20. The
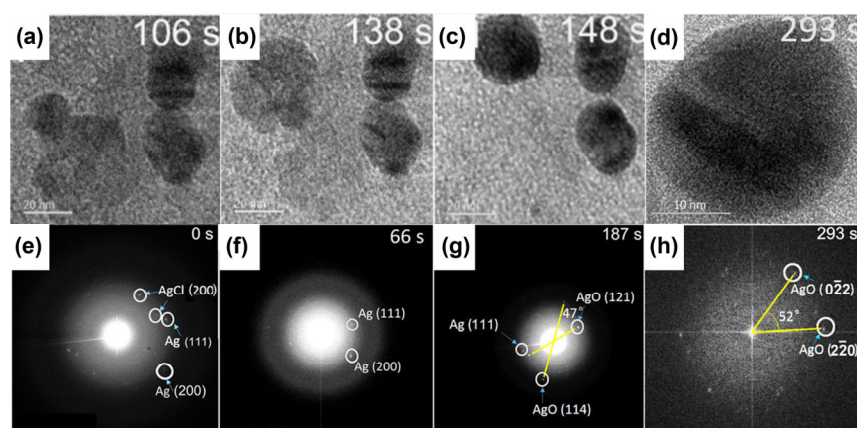

Figure 19 TEM images (a)–(d) and SAED (e) and (f) and FFT (h) patterns obtained during the Ag/AgCl oxidation process. Reproduced with permission from Ref. [178], © American Chemical Society 2016.
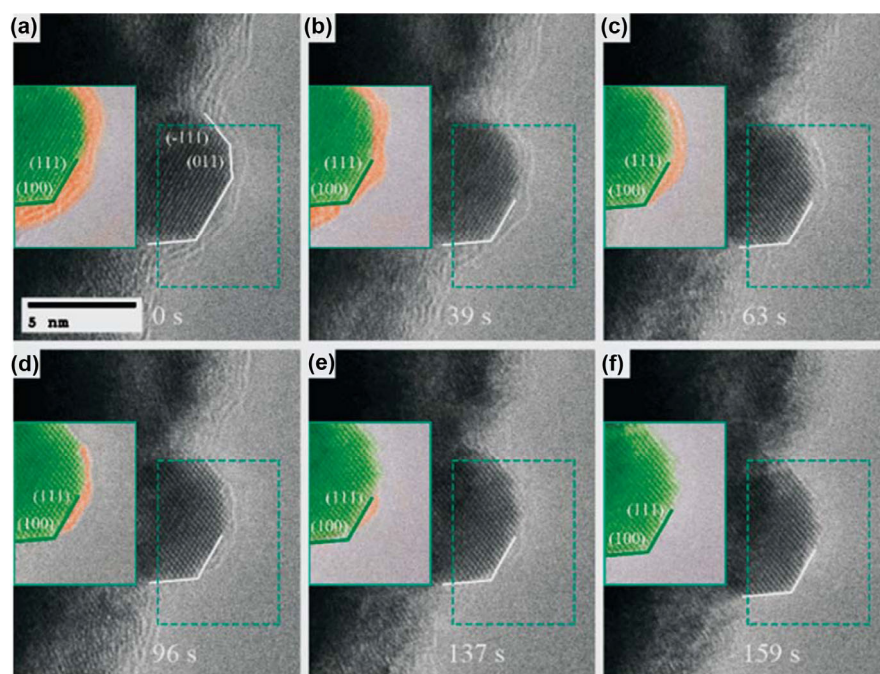

Figure 20 TEM images of the oxidation of graphene layers catalyzed by Pt NCs. Reproduced with permission from Ref. [162], © The Royal Society of Chemistry 2015.

graphene layers first ruptured on the edge between the (111) and (100) surfaces because of the low-coordination number atoms and abundant dangling bonds. After the rupturing on the edge, the stress was released, and the oxidation velocity was completely dependent on the facets. Quantitative analysis of the *in situ* TEM observations revealed that the oxidation on Pt (100) is faster than that on Pt (111), which is confirmed by similar quantification for other samples. Density functional theory calculations indicated that Pt (100) has an excellent ability to bind O_2 and O and dissociate O_2 into O, resulting in the high oxidation velocity.

Vendelbo et al. [20] used a gas flowing nanoreactor connected to a mass spectrometer to examine the Pt-catalyzed CO oxidation at 1 bar of pressure. The pressures of O_2, CO, and CO_2; the reaction power; and the shape factor in Figs. 21(a)–21(c) exhibit periodic variations with respect to time. As the CO conversion increased (CO pressure decreased), the spherical Pt NCs transformed into a faceted shape (Fig. 21(d)), terminated by the extended (111) surface. When the CO conversion decreased, the faceted Pt NCs transformed back to a spherical shape (Fig. 21(d)). This study directly demonstrated the dependency of the CO conversion on the Pt morphology.

5   Metal-failure mechanism

Another application of the controlled-atmosphere TEM techniques is to study the metal failure under various gaseous environments, such as hydrogen embrittlement and corrosion.

5.1   Hydrogen embrittlement

The deleterious effect of H on metals has been an important subject that has attracted considerable scientific and technological attention since the pioneering study of Johnson in 1875 [182]. Since 1980s, researchers have performed *in situ* studies on the H–metal interaction using electron microscopes with an environmental cell for numerous materials, such as Fe [183, 184], Ni [185], Al [186], and other related materials [187, 188]. They demonstrated that H could enhance the mobility of dislocations and increase the crack propagation rate. Recently, Xie et al. [50] exposed single-crystalline Al pillars with thin oxide layers to 2 Pa H_2 at room temperature to study the initial stage of H_2-induced interfacial failure. Figure 22 shows the cavity nucleation and growth below the Al/oxide interface. When H_2 ionized by the electron beam accumulated at the Al/oxide interface, the metal surface evolved into a thermodynamically
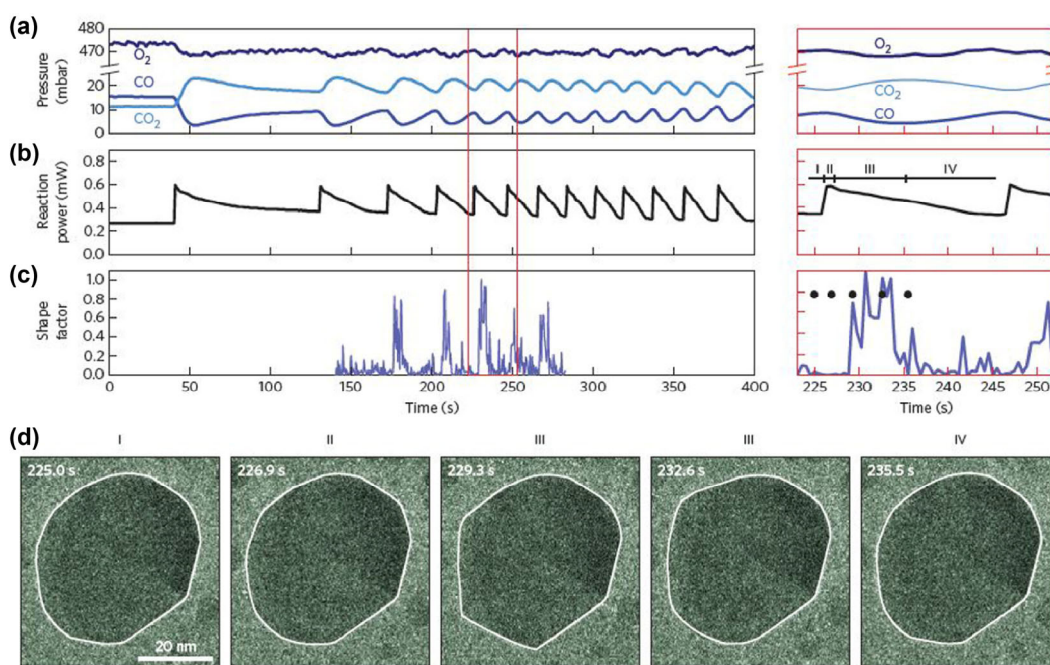

Figure 21   Evolution of the gas pressures (a), reaction power (b), shape factor (c), and morphology of a Pt NC (d) during a CO oxidation reaction. Reproduced with permission from Ref. [20], © Nature Publishing Group 2014.
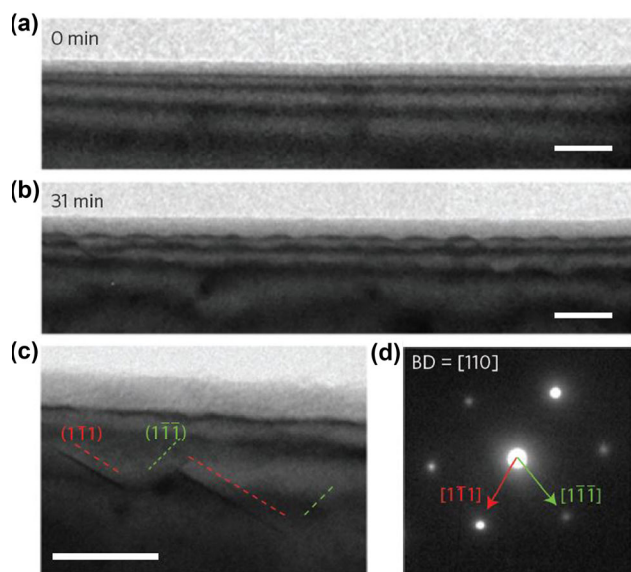
Figure 22 Cavity nucleation and growth (a) before and (b) after 31 min of exposure to H_2. (c) Close-up TEM image of the cavity. (d) SAED pattern along [110]. The scale bars represent 20 nm. Reproduced with permission from Ref. [50], © Nature Publishing Group 2015.

stable morphology following the Wulff construction. Considering the face-centered cubic crystalline structure of Al, the cavity was enclosed by (111) planes, as indicated in Figs. 22(c) and 22(d). After the cavity

reached a critical size, the oxide layer underwent plastic deformation and blistering on the surface, which caused the interfacial failure.

5.2 Corrosion

The application of metals is closely connected with their protection from corrosion in the working conditions, such as atmospheric and aqueous corrosion. Tremendous attention has been paid to the use of TEM to identify the structure and initialization of corrosion attacks [189–191], including quasi-*in situ* attempts. Both the atmospheric and aqueous corrosions can be investigated *in situ* via the closed-type approach. Malladi et al. [49] examined the localized corrosion in an Al alloy 2024-T3 by introducing O_2 bubbles that travelled through aqueous HCl into a nanoreactor, and *in situ* experiments were performed at a pressure of approximately 1.5 bar pressure and room temperature. Figure 23 illustrates two types of localized corrosion attacks in the Al alloy. After 5 h of exposure to the liquid–gas environment, the grain-boundary precipitate in location 1 (indicated by the blue arrows in Figs. 23(a) and 23(b)) disappeared owing to de-alloying, exhibiting an anodic nature, as shown in
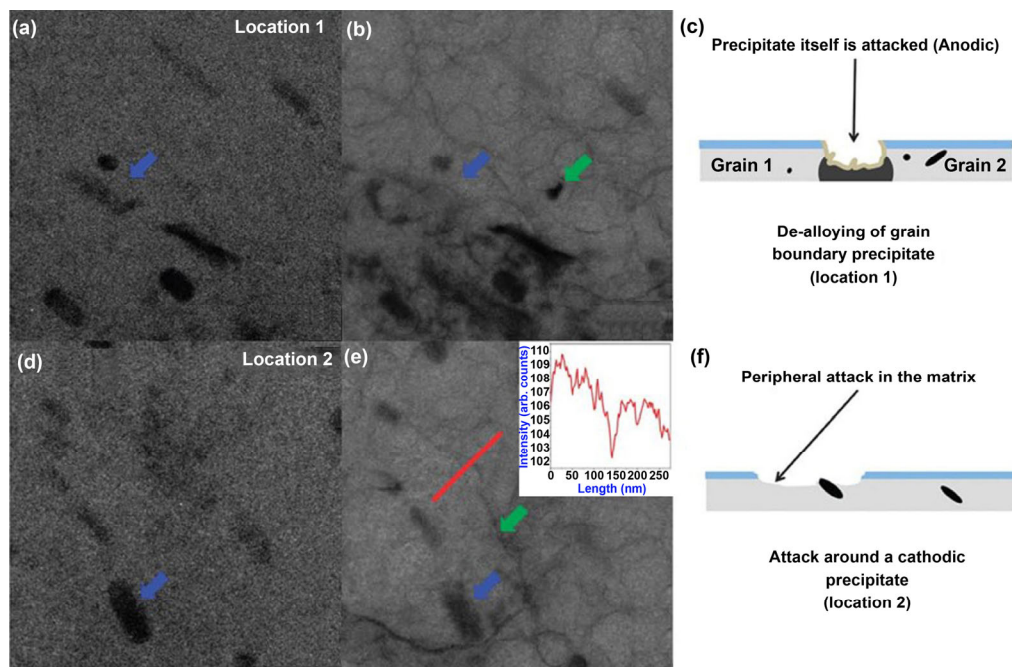

Figure 23 TEM images of location 1 (a) before and (b) after corrosion. (c) Schematic of the de-alloying of the grain-boundary precipitate. TEM images of location 2 (d) before and (e) after corrosion. (f) Schematic of the attack around the matrix precipitates. Reproduced with permission from Ref. [49], © The Royal Society of Chemistry 2013.

Fig. 23(c). In location 2, the peripheral attack emerging around the matrix precipitates (indicated by the blue arrows in Figs. 23(d) and 23(e)) exhibits the cathodic nature of the matrix precipitates (Fig. 23(f)).

Phase transition induced by gas species can be visualized *in situ* via controlled-atmosphere TEM, and remarkable achievements have been made, especially for the Pd–H system. Dionne's group and coworkers [51, 52] employed bulk plasmon resonance to identify the H absorption and desorption processes as well as the α/β phase transition inside an ETEM. The loading isotherms determined via electron energy-loss spectroscopy (EELS) demonstrated that single-crystalline Pd NCs absorb H abruptly and uniformly, whereas multiply twinned icosahedral NCs exclude H from the regions of high compressive strains.

6   Conclusions and outlook

The studies discussed in this review illustrate how the *in situ* TEM techniques allow us to monitor the active states of materials in gaseous atmospheres and represent the progress that researchers have made in the past few decades. By presenting the principles and highlighting recent results of our group and others, we demonstrated that this technique, i.e., using various adaptations of transmission electron microscopes or holders to establish a controlled atmosphere around the sample, allows the simulation of the realistic conditions of NW growth, catalysis, and metal failure and has undoubtedly revolutionized research in these areas. Remarkable understandings of the dynamics and kinetics of those processes have been obtained, which cannot be obtained using other techniques. However, controlled-atmosphere TEM poses technical challenges, such as accurately resolving the structure, dynamic monitoring, and combination with other external stimuli, which may introduce future research opportunities.

6.1   Structure resolving

Previously reported *in situ* experiments have demonstrated the ability of controlled-atmosphere TEM to image atoms via both the open and closed-type approaches; however, the accurate atomic structure on the surface is still difficult to identify in the gas nanoreactor owing to the electron scattering due to the gas layer and the bottom and top window films. Currently, the materials extensively adopted are carbon and silicon nitride with a thickness of 10–50 nm, and the height of the gas channel is < 1 mm. Finding ultrathin and small electron-scattering films for the windows and reducing the height of the gas channel are promising areas for improving the spatial resolution and the signal-to-noise ratio of the images.

Another issue in resolving the structure is obtaining chemical information about the materials inside the nanoreactor. According to the current geometrical design of the nanoreactor, X-rays generated by the electron-sample interaction are blocked by the top chip and other cover; thus, energy-dispersive X-ray spectroscopy is unsuitable for distinguishing the elements. Instead, other analytical methods, such as EELS and electron holography, attract continuous attentions for retrieving information about the elements, electric structure, and electric and magnetic fields in the sample. Chenna et al. [192] utilized EELS to quantify catalytic products at various temperatures during CO oxidation and CO_2 methanation, but this is still a challenge owing to the relatively long acquisition time and electron-beam damage.

6.2   Dynamic monitoring

Most of the previous experiments performed in the nanoreactor were static, and gas-flowing systems simulating real-world continuous reactions should be a focus of future research. Monitoring the structure and reactivity simultaneously in a continuous reaction, which is called operando analysis, is critical for establishing the structure–reactivity correlation. However, most gaseous reactants and products cannot be imaged via TEM, which restricts the quantification of the reactivity. For solid–gas reaction systems, such as graphene oxidation, the reactivity can be derived by quantifying the solid (graphene) evolution instead of the gas species; for the reactions where all the reactants and products are gaseous, extra analytical methods are needed to determine the catalytic activity. One technique is to apply the gas-flowing system together with on-line analytical methods (such as mass

spectrometry and gas chromatography) at the outlet of the nanoreactor, as shown in Fig. 1. Promising modifications for operando analysis are currently being investigated by our group.

Another crucial problem encountered in dynamic monitoring is the temporal resolution. Currently, most of the structure behaviors are determined with time-averaged observations. In particular, for catalytic reactions, it is impossible to resolve the fast gas–solid and electron interaction using the current TEM facilities. One typical reason is the low read-out frequency of the traditional charge-coupled device camera with a speed of ~ 30 frames per second. This has been significantly improved using complementary metal-oxide semiconductor and direct electron detection cameras, which allow imaging at 300–1,600 frames per second. However, the temporal resolution is still limited by the electron-beam current. A recently developed four-dimensional (ultrafast) transmission electron microscope using a short electron pulse with a high electron-beam current achieves a high temporal resolution, which can be 10 orders of magnitude higher than that of the conventional microscopes [193, 194].

6.3 Coupling with other external stimuli

Researchers have achieved tremendous success by coupling heating with controlled-atmosphere TEM in the fields of NW growth and catalysis. Interest in introducing other external stimuli into the atmosphere for examining the structure/composition evolution *in vivo* in a more complex and realistic environment is increasing. For example, quantitative mechanical loading on alloys in H_2/corrosive environments within a transmission electron microscope facilitates *in situ* studies on H embrittlement, stress corrosion, corrosion fatigue, etc. Xie et al. [195] studied the dislocation movement in hydrogenated/dehydrogenated Al, and found that the dislocation could be locked by the H-vacancy complexes. Coupling light and electrical biasing with controlled-atmosphere TEM may provide microscopic insight into the structure–property correlation in photosynthesis, lithium air batteries, and gas sensors. We believe that all of these couplings will spark further *in situ* studies, either involving functional holders in ETEMs or the design of "all-in-one" nanoreactors.

References

[1] Chen, M. S.; Goodman, D. W. Promotional effects of Au in Pd-Au catalysts for vinyl acetate synthesis. *Chinese J. Catal.* **2008**, *29*, 1178–1186.

[2] Edwards, J. K.; Freakley, S. J.; Lewis, R. J.; Pritchard, J. C.; Hutchings, G. J. Advances in the direct synthesis of hydrogen peroxide from hydrogen and oxygen. *Catal. Today* **2015**, *248*, 3–9.

[3] Keav, S.; Matam, S. K.; Ferri, D.; Weidenkaff, A. Structured perovskite-based catalysts and their application as three-way catalytic converters—A review. *Catalysts* **2014**, *4*, 226–255.

[4] Wang, J. H.; Chen, H.; Hu, Z. C.; Yao, M. F.; Li, Y. D. A review on the Pd-based three-way catalyst. *Catal. Rev.* **2015**, *57*, 79–144.

[5] Minh, N. Q. Ceramic fuel-cells. *J. Am. Ceram. Soc.* **1993**, *76*, 563–588.

[6] Adler, S. B. Factors governing oxygen reduction in solid oxide fuel cell cathodes. *Chem. Rev.* **2004**, *104*, 4791–4844.

[7] Mirzaei, A.; Janghorban, K.; Hashemi, B.; Neri, G. Metal-core@metal oxide-shell nanomaterials for gas-sensing applications: A review. *J. Nanopart. Res.* **2015**, *17*, 371.

[8] Zhang, J.; Liu, X. H.; Neri, G.; Pinna, N. Nanostructured materials for room-temperature gas sensors. *Adv. Mater.* **2016**, *28*, 795–831.

[9] Klenowicz, Z.; Darowicki, K. Waste incinerators: Corrosion problems and construction materials: A review. *Corros. Rev.* **2001**, *19*, 467–491.

[10] Venezuela, J.; Liu, Q. L.; Zhang, M. X.; Zhou, Q. J.; Atrens, A. A review of hydrogen embrittlement of martensitic advanced high-strength steels. *Corros. Rev.* **2016**, *34*, 153–186.

[11] Ren, J. T.; Tilley, R. D. Shape-controtled growth of platinum nanoparticles. *Small* **2007**, *3*, 1508–1512.

[12] Huang, X. Q.; Tang, S. H.; Mu, X. L.; Dai, Y.; Chen, G. X.; Zhou, Z. Y.; Ruan, F. X.; Yang, Z. L.; Zheng, N. F. Freestanding palladium nanosheets with plasmonic and catalytic properties. *Nat. Nanotechnol.* **2011**, *6*, 28–32.

[13] Dai, Y.; Mu, X. L.; Tan, Y. M.; Lin, K. Q.; Yang, Z. L.; Zheng, N. F.; Fu, G. Carbon monoxide-assisted synthesis of single-crystalline Pd tetrapod nanocrystals through hydride

formation. *J. Am. Chem. Soc.* **2012**, *134*, 7073–7080.

[14] Ahmadi, T. S.; Wang, Z. L.; Green, T. C.; Henglein, A.; El-Sayed, M. A. Shape-controlled synthesis of colloidal platinum nanoparticles. *Science* **1996**, *272*, 1924–1925.

[15] Mtangi, W.; Auret, F. D.; Meyer, W. E.; Legodi, M. J.; van Rensburg, P. J. J.; Coelho, S. M. M.; Diale, M.; Nel, J. M. Effects of hydrogen, oxygen, and argon annealing on the electrical properties of ZnO and ZnO devices studied by current-voltage, deep level transient spectroscopy, and Laplace DLTS. *J. Appl. Phys.* **2012**, *111*, 094504.

[16] Yu, W. Y.; Zhang, L.; Mullen, G. M.; Evans, E. J., Jr.; Henkelman, G.; Mullins, C. B. Effect of annealing in oxygen on alloy structures of Pd-Au bimetallic model catalysts. *Phys. Chem. Chem. Phys.* **2015**, *17*, 20588–20596.

[17] Over, H.; Kim, Y. D.; Seitsonen, A. P.; Wendt, S.; Lundgren, E.; Schmid, M.; Varga, P.; Morgante, A.; Ertl, G. Atomic-scale structure and catalytic reactivity of the RuO_2(110) surface. *Science* **2000**, *287*, 1474–1476.

[18] Yamauchi, M.; Tsukuda, T. Production of an ordered (B2) CuPd nanoalloy by low-temperature annealing under hydrogen atmosphere. *Dalton Trans.* **2011**, *40*, 4842–4845.

[19] Mouaddib, N.; Feumi-Jantou, C.; Garbowski, E.; Primet, M. Catalytic oxidation of methane over palladium supported on alumina: Influence of the oxygen-to-methane ratio. *Appl. Catal. A-Gen.* **1992**, *87*, 129–144.

[20] Vendelbo, S. B.; Elkjær, C. F.; Falsig, H.; Puspitasari, I.; Dona, P.; Mele, L.; Morana, B.; Nelissen, B. J.; van Rijn, R.; Creemer, J. F. et al. Visualization of oscillatory behaviour of Pt nanoparticles catalysing CO oxidation. *Nat. Mater.* **2014**, *13*, 884–890.

[21] Fujita, T.; Tokunaga, T.; Zhang, L.; Li, D. W.; Chen, L. Y.; Arai, S.; Yamamoto, Y.; Hirata, A.; Tanaka, N.; Ding, Y. et al. Atomic observation of catalysis-induced nanopore coarsening of nanoporous gold. *Nano Lett.* **2014**, *14*, 1172–1177.

[22] Sinclair, R. *In situ* high-resolution transmission electron microscopy of material reactions. *MRS Bull.* **2013**, *38*, 1065–1071.

[23] van Huis, M. A.; Kunneman, L. T.; Overgaag, K.; Xu, Q.; Pandraud, G.; Zandbergen, H. W.; Vanmaekelbergh, D. Low-temperature nanocrystal unification through rotations and relaxations probed by *in situ* transmission electron microscopy. *Nano Lett.* **2008**, *8*, 3959–3963.

[24] Jiang, Y.; Wang, Y.; Zhang, Y. Y.; Zhang, Z. F.; Yuan, W. T.; Sun, C. H.; Wei, X.; Brodsky, C. N.; Tsung, C. K.; Li, J. X. et al. Direct observation of Pt nanocrystal coalescence induced by electron-excitation-enhanced van der waals interactions. *Nano Res.* **2014**, *7*, 308–314.

[25] Benavidez, A. D.; Kovarik, L.; Genc, A.; Agrawal, N.; Larsson, E. M.; Hansen, T. W.; Karim, A. M.; Datye, A. K. Environmental transmission electron microscopy study of the origins of anomalous particle size distributions in supported metal catalysts. *ACS Catal.* **2012**, *2*, 2349–2356.

[26] Huang, J. Y.; Zhong, L.; Wang, C. M.; Sullivan, J. P.; Xu, W.; Zhang, L. Q.; Mao, S. X.; Hudak, N. S.; Liu, X. H.; Subramanian, A. et al. *In situ* observation of the electro-chemical lithiation of a single SnO_2 nanowire electrode. *Science* **2010**, *330*, 1515–1520.

[27] Liu, X. H.; Wang, J. W.; Huang, S.; Fan, F. F.; Huang, X.; Liu, Y.; Krylyuk, S.; Yoo, J.; Dayeh, S. A.; Davydov, A. V. et al. *In situ* atomic-scale imaging of electrochemical lithiation in silicon. *Nat. Nanotechnol.* **2012**, *7*, 749–756.

[28] Meister, S.; Kim, S.; Cha, J. J.; Wong, H. S. P.; Cui, Y. *In situ* transmission electron microscopy observation of nanostructural changes in phase-change memory. *ACS Nano* **2011**, *5*, 2742–2748.

[29] Han, X. D.; Zheng, K.; Zhang, Y. F.; Zhang, X. N.; Zhang, Z.; Wang, Z. L. Low-temperature *in situ* large-strain plasticity of silicon nanowires. *Adv. Mater.* **2007**, *19*, 2112–2118.

[30] Liu, P.; Mao, S. C.; Wang, L. H.; Han, X. D.; Zhang, Z. Direct dynamic atomic mechanisms of strain-induced grain rotation in nanocrystalline, textured, columnar-structured thin gold films. *Scr. Mater.* **2011**, *64*, 343–346.

[31] Wang, L. H.; Liu, P.; Guan, P. F.; Yang, M. J.; Sun, J. L.; Cheng, Y. Q.; Hirata, A.; Zhang, Z.; Ma, E.; Chen, M. W. et al. *In situ* atomic-scale observation of continuous and reversible lattice deformation beyond the elastic limit. *Nat. Commun.* **2013**, *4*, 2413.

[32] Yue, Y. H.; Chen, N. K.; Li, X. B.; Zhang, S. B.; Zhang, Z.; Chen, M. W.; Han, X. D. Crystalline liquid and rubber-like behavior in Cu nanowires. *Nano Lett.* **2013**, *13*, 3812–3816.

[33] Zhang, Y.; Han, X.; Zheng, K.; Zhang, Z.; Zhang, X.; Fu, J.; Ji, Y.; Hao, Y.; Guo, X.; Wang, Z. L. Direct observation of super-plasticity of beta-SiC nanowires at low temperature. *Adv. Funct. Mater.* **2007**, *17*, 3435–3440.

[34] Zheng, K.; Wang, C. C.; Cheng, Y. Q.; Yue, Y. H.; Han, X. D.; Zhang, Z.; Shan, Z. W.; Mao, S. X.; Ye, M. M.; Yin, Y. D. et al. Electron-beam-assisted superplastic shaping of nanoscale amorphous silica. *Nat. Commun.* **2010**, *1*, 24.

[35] Marton, L. La microscopie electronique des objets biologiques. *Bull. Acad. R. Belg. Cl. Sci.* **1935**, *21*, 553–564.

[36] Flower, H. M. High-voltage electron-microscopy of environmental reactions. *J. Microsc.* **1973**, *97*, 171–190.

[37] Sharma, R.; Crozier, P. A. Environmental transmission electron microscopy in nanotechnology. In *Handbook of Microscopy for Nanotechnology*; Yao, N.; Wang, Z. L., Eds.; Springer: New York, 2005; pp 531–565.

[38] Gai, P. L.; Boyes, E. D.; Helveg, S.; Hansen, P. L.; Giorgio, S.; Henry, C. R. Atomic-resolution environmental transmission electron microscopy for probing gas-solid reactions in heterogeneous catalysis. *MRS Bull.* **2007**, *32*, 1044–1050.

[39] Tao, F. F.; Crozier, P. A. Atomic-scale observations of catalyst structures under reaction conditions and during catalysis. *Chem. Rev.* **2016**, *116*, 3487–3539.

[40] Jinschek, J. R. Advances in the environmental transmission electron microscope (ETEM) for nanoscale *in situ* studies of gas–solid interactions. *Chem. Commun.* **2014**, *50*, 2696–2706.

[41] Takeda, S.; Yoshida, H. Atomic-resolution environmental TEM for quantitative *in-situ* microscopy in materials science. *Microscopy* **2013**, *62*, 193–203.

[42] Zhang, S. R.; Nguyen, L.; Zhu, Y.; Zhan, S. H.; Tsung, C. K.; Tao, F. *In-situ* studies of nanocatalysis. *Acc. Chem. Res.* **2013**, *46*, 1731–1739.

[43] Hansen, T. W.; Wagner, J. B. *Controlled Atmosphere Transmission Electron Microscopy*; Springer International Publishing: Switzerland, 2016.

[44] Taheri, M. L.; Stach, E. A.; Arslan, I.; Crozier, P. A.; Kabius, B. C.; LaGrange, T.; Minor, A. M.; Takeda, S.; Tanase, M.; Wagner, J. B. et al. Current status and future directions for *in situ* transmission electron microscopy. *Ultramicroscopy* **2016**, *170*, 86–95.

[45] Alsem, D.; Salmon, N. J.; Unocic, R. R.; Veith, G. M.; More, K. L. *In-situ* liquid and gas transmission electron microscopy of nano-scale materials. *Microsc. Microanal.* **2012**, *18*, 1158–1159.

[46] Panciera, F.; Norton, M. M.; Alam, S. B.; Hofmann, S.; Mølhave, K.; Ross, F. M. Controlling nanowire growth through electric field-induced deformation of the catalyst droplet. *Nat. Commun.* **2016**, *7*, 12271.

[47] Ross, F. M. Controlling nanowire structures through real time growth studies. *Rep. Prog. Phys.* **2010**, *73*, 114501.

[48] Helveg, S.; López-Cartes, C.; Sehested, J.; Hansen, P. L.; Clausen, B. S.; Rostrup-Nielsen, J. R.; Abild-Pedersen, F.; Nørskov, J. K. Atomic-scale imaging of carbon nanofibre growth. *Nature* **2004**, *427*, 426–429.

[49] Malladi, S.; Shen, C. G.; Xu, Q.; de Kruijff, T.; Yücelen, E.; Tichelaar, F.; Zandbergen, H. Localised corrosion in aluminium alloy 2024-T3 using *in situ* TEM. *Chem. Commun.* **2013**, *49*, 10859–10861.

[50] Xie, D. G.; Wang, Z. J.; Sun, J.; Li, J.; Ma, E.; Shan, Z. W. *In situ* study of the initiation of hydrogen bubbles at the aluminium metal/oxide interface. *Nat. Mater.* **2015**, *14*, 899–903.

[51] Baldi, A.; Narayan, T. C.; Koh, A. L.; Dionne, J. A. *In situ* detection of hydrogen-induced phase transitions in individual palladium nanocrystals. *Nat. Mater.* **2014**, *13*, 1143–1148.

[52] Narayan, T. C.; Baldi, A.; Koh, A. L.; Sinclair, R.; Dionne, J. A. Reconstructing solute-induced phase transformations within individual nanocrystals. *Nat. Mater.* **2016**, *15*, 768–774.

[53] Crozier, P. A.; Sharma, R.; Datye, A. K. Oxidation and reduction of small palladium particles on silica. *Microsc. Microanal.* **1998**, *4*, 278–285.

[54] Koh, A. L.; Gidcumb, E.; Zhou, O.; Sinclair, R. Observations of carbon nanotube oxidation in an aberration-corrected environmental transmission electron microscope. *ACS Nano* **2013**, *7*, 2566–2572.

[55] Sun, L.; Noh, K. W.; Wen, J.-G.; Dillon, S. J. *In situ* transmission electron microscopy observation of silver oxidation in ionized/atomic gas. *Langmuir* **2011**, *27*, 14201–14206.

[56] Yokosawa, T.; Tichelaar, F. D.; Zandbergen, H. W. *In-situ* TEM on epitaxial and non-epitaxial oxidation of Pd and reduction of PdO at $P = 0.2$–0.7 bar and $T = 20$–650 °C. *Eur. J. Inorg. Chem.* **2016**, *2016*, 3094–3102.

[57] Yoshida, H.; Omote, H.; Takeda, S. Oxidation and reduction processes of platinum nanoparticles observed at the atomic scale by environmental transmission electron microscopy. *Nanoscale* **2014**, *6*, 13113–13118.

[58] Zhou, G. W.; Luo, L. L.; Li, L.; Ciston, J.; Stach, E. A.; Saidi, W. A.; Yang, J. C. *In situ* atomic-scale visualization of oxide islanding during oxidation of Cu surfaces. *Chem. Commun.* **2013**, *49*, 10862–10864.

[59] LaGrow, A. P.; Ward, M. R.; Lloyd, D. C.; Gai, P. L.; Boyes, E. D. Visualizing the Cu/Cu$_2$O interface transition in nanoparticles with environmental scanning transmission electron microscopy. *J. Am. Chem. Soc.* **2017**, *139*, 179–185.

[60] Zhang, X. F.; Kamino, T. Imaging gas–solid interactions in an atomic resolution environmental TEM. *Microsc. Today* **2006**, *14*, 16–18.

[61] Boyes, E. D.; Gai, P. L. Environmental high resolution electron microscopy and applications to chemical science. *Ultramicroscopy* **1997**, *67*, 219–232.

[62] Gai, P. L.; Kourtakis, K.; Ziemecki, S. *In situ* real-time environmental high resolution electron microscopy of nanometer size novel xerogel catalysts for hydrogenation reactions in Nylon 6, 6. *Microsc. Microanal.* **2000**, *6*, 335–342.

[63] Kamino, T.; Yaguchi, T.; Konno, M.; Watabe, A.; Marukawa, T.; Mima, T.; Kuroda, K.; Saka, H.; Arai, S.; Makino, H. et al. Development of a gas injection/specimen heating holder for use with transmission electron microscope. *J. Electron Microsc.* **2005**, *54*, 497–503.

[64] Jinschek, J. R.; Helveg, S. Image resolution and sensitivity

in an environmental transmission electron microscope. *Micron* **2012**, *43*, 1156–1168.

[65] Creemer, J. F.; Helveg, S.; Hoveling, G. H.; Ullmann, S.; Molenbroek, A. M.; Sarro, P. M.; Zandbergen, H. W. Atomic-scale electron microscopy at ambient pressure. *Ultramicroscopy* **2008**, *108*, 993–998.

[66] Pérez Garza, H. H.; Morsink, D.; Xu, J.; Sholkina, M.; Pivak, Y.; Pen, M.; van Weperen, S.; Xu, Q. MEMS-based nanoreactor for *in situ* analysis of solid–gas interactions inside the transmission electron microscope. *Micro Nano Lett.* **2017**, *12*, 69–75.

[67] Li, D. S.; Nielsen, M. H.; De Yoreo, J. J. Design, fabrication, and applications of *in situ* fluid cell TEM. In *Research Methods in Biomineralization Science*; De Yoreo, J. J., Ed.; Academic Press Inc.: San Diego, 2013; pp 147–164.

[68] de Jonge, N.; Pfaff, M.; Peckys, D. B. Practical aspects of transmission electron microscopy in liquid. In *Advances in Imaging and Electron Physics*; Hawkes, P. W., Ed.; Academic Press Inc.: San Diego, 2014; Vol. 186, pp 1–37.

[69] Liao, H. G.; Zheng, H. M. Liquid cell transmission electron microscopy. *Annu. Rev. Phys. Chem.* **2016**, *67*, 719–747.

[70] de Jonge, N.; Ross, F. M. Electron microscopy of specimens in liquid. *Nat. Nanotechnol.* **2011**, *6*, 695–704.

[71] Yokosawa, T.; Alan, T.; Pandraud, G.; Dam, B.; Zandbergen, H. *In-situ* TEM on (de)hydrogenation of Pd at 0.5–4.5 bar hydrogen pressure and 20–400 °C. *Ultramicroscopy* **2012**, *112*, 47–52.

[72] Yaguchi, T.; Suzuki, M.; Watabe, A.; Nagakubo, Y.; Ueda, K.; Kamino, T. Development of a high temperature-atmospheric pressure environmental cell for high-resolution TEM. *J. Electron Microsc.* **2011**, *60*, 217–225.

[73] Giorgio, S.; Sao Joao, S.; Nitsche, S.; Chaudanson, D.; Sitja, G.; Henry, C. R. Environmental electron microscopy (ETEM) for catalysts with a closed E-cell with carbon windows. *Ultramicroscopy* **2006**, *106*, 503–507.

[74] de Jonge, N.; Bigelow, W. C.; Veith, G. M. Atmospheric pressure scanning transmission electron microscopy. *Nano Lett.* **2010**, *10*, 1028–1031.

[75] Xin, H. L.; Niu, K. Y.; Alsem, D. H.; Zheng, H. M. *In situ* TEM study of catalytic nanoparticle reactions in atmospheric pressure gas environment. *Microsc. Microanal.* **2013**, *19*, 1558–1568.

[76] Mehraeen, S.; McKeown, J. T.; Deshmukh, P. V.; Evans, J. E.; Abellan, P.; Xu, P. H.; Reed, B. W.; Taheri, M. L.; Fischione, P. E.; Browning, N. D. A (S)TEM gas cell holder with localized laser heating for *in situ* experiments. *Microsc. Microanal.* **2013**, *19*, 470–478.

[77] Alan, T.; Yokosawa, T.; Gaspar, J.; Pandraud, G.; Paul, O.; Creemer, F.; Sarro, P. M.; Zandbergen, H. W. Micro-

fabricated channel with ultra-thin yet ultra-strong windows enables electron microscopy under 4-bar pressure. *Appl. Phys. Lett.* **2012**, *100*, 081903.

[78] Ueda, K.; Kawasaki, T.; Hasegawa, H.; Tanji, T.; Ichihashi, M. First observation of dynamic shape changes of a gold nanoparticle catalyst under reaction gas environment by transmission electron microscopy. *Surf. Interface Anal.* **2008**, *40*, 1725–1727.

[79] Yang, J. L.; Paul, O. Fracture properties of LPCVD silicon nitride thin films from the load-deflection of long membranes. *Sensor. Actuat. A-Phys.* **2002**, *97–98*, 520–526.

[80] Wakasugi, T.; Isobe, S.; Umeda, A.; Wang, Y. M.; Hashimoto, N.; Ohnuki, S. Development and application of a window-type environmental cell in high voltage electron microscope. *J. Alloys Compd.* **2013**, *580*, S127–S130.

[81] McDonald, M. L.; Gibson, J. M.; Unterwald, F. C. Design of an ultrahigh-vacuum specimen environment for high-resolution transmission electron microscopy. *Rev. Sci. Instrum.* **1989**, *60*, 700–707.

[82] Hammar, M.; LeGoues, F. K.; Tersoff, J.; Reuter, M. C.; Tromp, R. M. *In situ* ultrahigh vacuum transmission electron microscopy studies of hetero-epitaxial growth. I. Si(001)/ Ge. *Surf. Sci.* **1996**, *349*, 129–144.

[83] Wu, Y. Y.; Yang, P. D. Direct observation of vapor-liquid-solid nanowire growth. *J. Am. Chem. Soc.* **2001**, *123*, 3165–3166.

[84] Stach, E. A.; Pauzauskie, P. J.; Kuykendall, T.; Goldberger, J.; He, R. R.; Yang, P. D. Watching GaN nanowires grow. *Nano Lett.* **2003**, *3*, 867–869.

[85] Taheri, M. L.; Reed, B. W.; LaGrange, T. B.; Browning, N. D. *In situ* laser synthesis of Si nanowires in the dynamic TEM. *Small* **2008**, *4*, 2187–2190.

[86] Wagner, R. S.; Ellis, W. C. Vapor-liquid-solid mechanism of single crystal growth. *Appl. Phys. Lett.* **1964**, *4*, 89–90.

[87] Kim, B. J.; Tersoff, J.; Wen, C. Y.; Reuter, M. C.; Stach, E. A.; Ross, F. M. Determination of size effects during the phase transition of a nanoscale Au-Si eutectic. *Phys. Rev. Lett.* **2009**, *103*, 155701.

[88] Kim, B. J.; Tersoff, J.; Kodambaka, S.; Reuter, M. C.; Stach, E. A.; Ross, F. M. Kinetics of individual nucleation events observed in nanoscale vapor-liquid-solid growth. *Science* **2008**, *322*, 1070–1073.

[89] Li, A.; Sibirev, N. V.; Ercolani, D.; Dubrovskii, V. G.; Sorba, L. Readsorption assisted growth of InAs/InSb heterostructured nanowire arrays. *Cryst. Growth Des.* **2013**, *13*, 878–882.

[90] Ross, F. M.; Tersoff, J.; Reuter, M. C. Sawtooth faceting in silicon nanowires. *Phys. Rev. Lett.* **2005**, *95*, 146104.

[91] Hannon, J. B.; Kodambaka, S.; Ross, F. M.; Tromp, R. M.

The influence of the surface migration of gold on the growth of silicon nanowires. *Nature* **2006**, *440*, 69–71.

[92] Kodambaka, S.; Hannon, J. B.; Tromp, R. M.; Ross, F. M. Control of Si nanowire growth by oxygen. *Nano Lett.* **2006**, *6*, 1292–1296.

[93] Schwarz, K. W.; Tersoff, J. Elementary processes in nanowire growth. *Nano Lett.* **2011**, *11*, 316–320.

[94] Kodambaka, S.; Tersoff, J.; Reuter, M. C.; Ross, F. M. Germanium nanowire growth below the eutectic temperature. *Science* **2007**, *316*, 729–732.

[95] Gamalski, A. D.; Tersoff, J.; Kodambaka, S.; Zakharov, D. N.; Ross, F. M.; Stach, E. A. The role of surface passivation in controlling Ge nanowire faceting. *Nano Lett.* **2015**, *15*, 8211–8216.

[96] Diaz, R. E.; Sharma, R.; Jarvis, K.; Zhang, Q. L.; Mahajan, S. Direct observation of nucleation and early stages of growth of GaN nanowires. *J. Cryst. Growth* **2012**, *341*, 1–6.

[97] Gamalski, A. D.; Tersoff, J.; Stach, E. A. Atomic resolution *in situ* imaging of a double-bilayer multistep growth mode in gallium nitride nanowires. *Nano Lett.* **2016**, *16*, 2283–2288.

[98] Chou, Y. C.; Hillerich, K.; Tersoff, J.; Reuter, M. C.; Dick, K. A.; Ross, F. M. Atomic-scale variability and control of III-V nanowire growth kinetics. *Science* **2014**, *343*, 281–284.

[99] Wen, C. Y.; Tersoff, J.; Hillerich, K.; Reuter, M. C.; Park, J. H.; Kodambaka, S.; Stach, E. A.; Ross, F. M. Periodically changing morphology of the growth interface in Si, Ge, and GaP nanowires. *Phys. Rev. Lett.* **2011**, *107*, 025503.

[100] Lenrick, F.; Ek, M.; Deppert, K.; Samuelson, L.; Reine Wallenberg, L. Straight and kinked InAs nanowire growth observed *in situ* by transmission electron microscopy. *Nano Res.* **2014**, *7*, 1188–1194.

[101] Hofmann, S.; Sharma, R.; Wirth, C. T.; Cervantes-Sodi, F.; Ducati, C.; Kasama, T.; Dunin-Borkowski, R. E.; Drucker, J.; Bennett, P.; Robertson, J. Ledge-flow-controlled catalyst interface dynamics during Si nanowire growth. *Nat. Mater.* **2008**, *7*, 372–375.

[102] Wen, C. Y.; Reuter, M. C.; Bruley, J.; Tersoff, J.; Kodambaka, S.; Stach, E. A.; Ross, F. M. Formation of compositionally abrupt axial heterojunctions in silicon-germanium nanowires. *Science* **2009**, *326*, 1247–1250.

[103] Wen, C. Y.; Reuter, M. C.; Tersoff, J.; Stach, E. A.; Ross, F. M. Structure, growth kinetics, and ledge flow during vapor-solid-solid growth of copper-catalyzed silicon nanowires. *Nano Lett.* **2010**, *10*, 514–519.

[104] Chou, Y. C.; Wen, C. Y.; Reuter, M. C.; Su, D.; Stach, E. A.; Ross, F. M. Controlling the growth of Si/Ge nanowires and heterojunctions using silver-gold alloy catalysts. *ACS Nano* **2012**, *6*, 6407–6415.

[105] Chou, Y. C.; Panciera, F.; Reuter, M. C.; Stach, E. A.; Ross, F. M. Nanowire growth kinetics in aberration corrected environmental transmission electron microscopy. *Chem. Commun.* **2016**, *52*, 5686–5689.

[106] Chen, C. L.; Mori, H. *In situ* TEM observation of the growth and decomposition of monoclinic $W_{18}O_{49}$ nanowires. *Nanotechnology* **2009**, *20*, 285604.

[107] Tokunaga, T.; Kawamoto, T.; Tanaka, K.; Nakamura, N.; Hayashi, Y.; Sasaki, K.; Kuroda, K.; Yamamoto, T. Growth and structure analysis of tungsten oxide nanorods using environmental TEM. *Nanoscale Res. Lett.* **2012**, *7*, 85.

[108] Duchstein, L. D. L.; Damsgaard, C. D.; Hansen, T. W.; Wagner, J. B. Low-pressure ETEM studies of Au assisted MgO nanorod growth. *J. Phys.* **2014**, *522*, 012010.

[109] Rackauskas, S.; Jiang, H.; Wagner, J. B.; Shandakov, S. D.; Hansen, T. W.; Kauppinen, E. I.; Nasibulin, A. G. *In situ* study of noncatalytic metal oxide nanowire growth. *Nano Lett.* **2014**, *14*, 5810–5813.

[110] Kodambaka, S.; Tersoff, J.; Reuter, M. C.; Ross, F. M. Diameter-independent kinetics in the vapor-liquid-solid growth of Si nanowires. *Phys. Rev. Lett.* **2006**, *96*, 096105.

[111] Wen, C. Y.; Tersoff, J.; Reuter, M. C.; Stach, E. A.; Ross, F. M. Step-flow kinetics in nanowire growth. *Phys. Rev. Lett.* **2010**, *105*, 195502.

[112] Schwarz, K. W.; Tersoff, J.; Kodambaka, S.; Ross, F. M. Jumping-catalyst dynamics in nanowire growth. *Phys. Rev. Lett.* **2014**, *113*, 055501.

[113] Kolibal, M.; Vystavěl, T.; Varga, P.; Šikola, T. Real-time observation of collector droplet oscillations during growth of straight nanowires. *Nano Lett.* **2014**, *14*, 1756–1761.

[114] Oh, S. H.; Chisholm, M. F.; Kauffmann, Y.; Kaplan, W. D.; Luo, W. D.; Rühle, M.; Scheu, C. Oscillatory mass transport in vapor-liquid-solid growth of sapphire nanowires. *Science* **2010**, *330*, 489–493.

[115] Gamalski, A. D.; Ducati, C.; Hofmann, S. Cyclic supersaturation and triple phase boundary dynamics in germanium nanowire growth. *J. Phys. Chem. C* **2011**, *115*, 4413–4417.

[116] Zhang, Z. F.; Wang, Y.; Li, H. B.; Yuan, W. T.; Zhang, X. F.; Sun, C. H.; Zhang, Z. Atomic-scale observation of vapor–solid nanowire growth via oscillatory mass transport. *ACS Nano* **2016**, *10*, 763–769.

[117] Zhang, Z. F.; Chen, J. L.; Li, H. B.; Zhang, Z.; Wang, Y. Vapor–solid nanotube growth via sidewall epitaxy in an environmental transmission electron microscope. *Cryst. Growth Des.* **2017**, *17*, 11–15.

[118] Schwarz, K. W.; Tersoff, J. From droplets to nanowires: Dynamics of vapor-liquid-solid growth. *Phys. Rev. Lett.* **2009**, *102*, 206101.

[119] Tersoff, J.; Denier van der Gon, A. W.; Tromp, R. M.

Shape oscillations in growth of small crystals. *Phys. Rev. Lett.* **1993**, *70*, 1143–1146.

[120] Yuan, W. T.; Yu, J.; Li, H. B.; Zhang, Z.; Sun, C. H.; Wang, Y. *In situ* TEM observation of dissolution and regrowth dynamics of MoO$_2$ nanowires under oxygen. *Nano Res.* **2017**, *10*, 397–404.

[121] Madras, P.; Dailey, E.; Drucker, J. Kinetically induced kinking of vapor−liquid−solid grown epitaxial Si nanowires. *Nano Lett.* **2009**, *9*, 3826–3830.

[122] Hillerich, K.; Dick, K. A.; Wen, C. Y.; Reuter, M. C.; Kodambaka, S.; Ross, F. M. Strategies to control morphology in hybrid group III-V/group IV heterostructure nanowires. *Nano Lett.* **2013**, *13*, 903–908.

[123] Schwarz, K. W.; Tersoff, J. Multiplicity of steady modes of nanowire growth. *Nano Lett.* **2012**, *12*, 1329–1332.

[124] Dick, K. A.; Kodambaka, S.; Reuter, M. C.; Deppert, K.; Samuelson, L.; Seifert, W.; Wallenberg, L. R.; Ross, F. M. The morphology of axial and branched nanowire heterostructures. *Nano Lett.* **2007**, *7*, 1817–1822.

[125] Panciera, F.; Chou, Y. C.; Reuter, M. C.; Zakharov, D.; Stach, E. A.; Hofmann, S.; Ross, F. M. Synthesis of nano-structures in nanowires using sequential catalyst reactions. *Nat. Mater.* **2015**, *14*, 820–825.

[126] Glas, F.; Harmand, J. C.; Patriarche, G. Why does wurtzite form in nanowires of III-V zinc blende semiconductors? *Phys. Rev. Lett.* **2007**, *99*, 146101.

[127] Lehmann, S.; Wallentin, J.; Jacobsson, D.; Deppert, K.; Dick, K. A. A general approach for sharp crystal phase switching in InAs, GaAs, InP, and GaP nanowires using only group V flow. *Nano Lett.* **2013**, *13*, 4099–4105.

[128] Assali, S.; Gagliano, L.; Oliveira, D. S.; Verheijen, M. A.; Plissard, S. R.; Feiner, L. F.; Bakkers, E. P. A. M. Exploring crystal phase switching in GaP nanowires. *Nano Lett.* **2015**, *15*, 8062–8069.

[129] Li, A.; Zou, J.; Han, X. D. Growth of III-V semiconductor nanowires and their heterostructures. *Sci. China-Mater.* **2016**, *59*, 51–91.

[130] Dubrovskii, V. G. Influence of the group V element on the chemical potential and crystal structure of Au-catalyzed III-V nanowires. *Appl. Phys. Lett.* **2014**, *104*, 053110.

[131] Jacobsson, D.; Panciera, F.; Tersoff, J.; Reuter, M. C.; Lehmann, S.; Hofmann, S.; Dick, K. A.; Ross, F. M. Interface dynamics and crystal phase switching in GaAs nanowires. *Nature* **2016**, *531*, 317–322.

[132] Su, D. S.; Zhang, B. S.; Schlögl, R. Electron microscopy of solid catalysts-transforming from a challenge to a toolbox. *Chem. Rev.* **2015**, *115*, 2818–2882.

[133] Akita, T.; Kohyama, M.; Haruta, M. Electron microscopy study of gold nanoparticles deposited on transition metal oxides. *Acc. Chem. Res.* **2013**, *46*, 1773–1782.

[134] Friedrich, H.; de Jongh, P. E.; Verkleij, A. J.; de Jong, K. P. Electron tomography for heterogeneous catalysts and related nanostructured materials. *Chem. Rev.* **2009**, *109*, 1613–1629.

[135] Liu, J. Advanced electron microscopy of metal-support interactions in supported metal catalysts. *ChemCatChem* **2011**, *3*, 934–948.

[136] Datye, A. K. Electron microscopy of catalysts: Recent achievements and future prospects. *J. Catal.* **2003**, *216*, 144–154.

[137] Gai, P. L. Developments of electron microscopy methods in the study of catalysts. *Curr. Opin. Solid State Mater. Sci.* **2001**, *5*, 371–380.

[138] Zhou, W.; Wachs, I. E.; Kiely, C. J. Nanostructural and chemical characterization of supported metal oxide catalysts by aberration corrected analytical electron microscopy. *Curr. Opin. Solid State Mater. Sci.* **2012**, *16*, 10–22.

[139] Ertl, G.; Knözinger, H.; Schüth, F.; Weitkamp, J. *Handbook of Heterogeneous Catalysis*; John Wiley and Sons, Inc.: Weinheim, 1997.

[140] Baker, R. T. K.; Harris, P. S.; Thomas, R. B. Direct observation of particle mobility on a surface in a gaseous environment. *Surf. Sci.* **1974**, *46*, 311–316.

[141] Baker, R. T. K.; Thomas, C.; Thomas, R. B. Continuous observation of the particle size behavior of platinum on alumina. *J. Catal.* **1975**, *38*, 510–513.

[142] Gai, P. L.; Boyes, E. D. Environmental high resolution electron microscopy in materials science. In *In-situ Microscopy in Materials Research: Leading International Research in Electron and Scanning Probe Microscopies*; Gai, P. L., Ed.; Springer: New York, 1997; pp 123–147.

[143] Liu, R.-J.; Crozier, P. A.; Smith, C. M.; Hucul, D. A.; Blackson, J.; Salaita, G. *In situ* electron microscopy studies of the sintering of palladium nanoparticles on alumina during catalyst regeneration processes. *Microsc. Microanal.* **2004**, *10*, 77–85.

[144] Simonsen, S. B.; Chorkendorff, I.; Dahl, S.; Skoglundh, M.; Sehested, J.; Helveg, S. Direct observations of oxygen-induced platinum nanoparticle ripening studied by *in situ* TEM. *J. Am. Chem. Soc.* **2010**, *132*, 7968–7975.

[145] Simonsen, S. B.; Chorkendorff, I.; Dahl, S.; Skoglundh, M.; Sehested, J.; Helveg, S. Ostwald ripening in a Pt/SiO$_2$ model catalyst studied by *in situ* TEM. *J. Catal.* **2011**, *281*, 147–155.

[146] Di Vece, M.; Bals, S.; Verbeeck, J.; Lievens, P.; Van Tendeloo, G. Compositional changes of Pd-Au bimetallic nanoclusters upon hydrogenation. *Phys. Rev. B* **2009**, *80*, 125420.

[147] Wang, Z. L.; Shapiro, A. J. Energy-filtering and composition-sensitive imaging in surface and interface studies using HREM. *Ultramicroscopy* **1995**, *60*, 115–135.

[148] Williams, E. D.; Marks, L. D. New and emerging techniques for imaging surfaces. *Crit. Rev. Surf. Chem.* **1995**, *5*, 275–303.

[149] Yu, R.; Hu, L. H.; Cheng, Z. Y.; Li, Y. D.; Ye, H. Q.; Zhu, J. Direct subangstrom measurement of surfaces of oxide particles. *Phys. Rev. Lett.* **2010**, *105*, 226101.

[150] Grozea, D.; Landree, E.; Collazo-Davila, C.; Bengu, E.; Plass, R.; Marks, L. D. Structural investigations of metal-semiconductor surfaces. *Micron* **1999**, *30*, 41–49.

[151] Chang, T. Y.; Tanaka, Y.; Ishikawa, R.; Toyoura, K.; Matsunaga, K.; Ikuhara, Y.; Shibata, N. Direct imaging of Pt single atoms adsorbed on TiO_2 (110) surfaces. *Nano Lett.* **2014**, *14*, 134–138.

[152] Eng, P. J.; Trainor, T. P.; Brown, G. E., Jr.; Waychunas, G. A.; Newville, M.; Sutton, S. R.; Rivers, M. L. Structure of the hydrated α-Al_2O_3 (0001) surface. *Science* **2000**, *288*, 1029–1033.

[153] Barth, C.; Reichling, M. Imaging the atomic arrangements on the high-temperature reconstructed α-Al_2O_3(0001) surface. *Nature* **2001**, *414*, 54–57.

[154] Liu, P.; Kendelewicz, T.; Brown, G. E., Jr.; Nelson, E. J.; Chambers, S. A. Reaction of water vapor with α-Al_2O_3(0001) and α-Fe_2O_3(0001) surfaces: Synchrotron X-ray photoemission studies and thermodynamic calculations. *Surf. Sci.* **1998**, *417*, 53–65.

[155] Tao, F.; Dag, S.; Wang, L.-W.; Liu, Z.; Butcher, D. R.; Bluhm, H.; Salmeron, M.; Somorjai, G. A. Break-up of stepped platinum catalyst surfaces by high CO coverage. *Science* **2010**, *327*, 850–853.

[156] Fujita, T.; Guan, P. F.; McKenna, K.; Lang, X. Y.; Hirata, A.; Zhang, L.; Tokunaga, T.; Arai, S.; Yamamoto, Y.; Tanaka, N. et al. Atomic origins of the high catalytic activity of nanoporous gold. *Nat. Mater.* **2012**, *11*, 775–780.

[157] Yoshida, H.; Kuwauchi, Y.; Jinschek, J. R.; Sun, K. J.; Tanaka, S.; Kohyama, M.; Shimada, S.; Haruta, M.; Takeda, S. Visualizing gas molecules interacting with supported nanoparticulate catalysts at reaction conditions. *Science* **2012**, *335*, 317–319.

[158] Tanner, R. E.; Sasahara, A.; Liang, Y.; Altman, E. I.; Onishi, H. Formic acid adsorption on anatase TiO_2(001)−(1 × 4) thin films studied by NC-AFM and STM. *J. Phys. Chem. B* **2002**, *106*, 8211–8222.

[159] Wang, Y.; Sun, H. J.; Tan, S. J.; Feng, H.; Cheng, Z. W.; Zhao, J.; Zhao, A. D.; Wang, B.; Luo, Y.; Yang, J. L. et al. Role of point defects on the reactivity of reconstructed anatase titanium dioxide (001) surface. *Nat. Commun.* **2013**, *4*, 2214.

[160] Li, H. B.; Yuan, W. T.; Jiang, Y.; Zhang, Z. F.; Zhang, Z.; Wang, Y. Observation of Pt-{100}-p(2×2)-O reconstruction by an environmental TEM. *Prog. Nat. Sci.* **2016**, *26*, 308–311.

[161] Yuan, W. T.; Wang, Y.; Li, H. B.; Wu, H. L.; Zhang, Z.; Selloni, A.; Sun, C. H. Real-time observation of reconstruction dynamics on TiO_2(001) surface under oxygen via an environmental transmission electron microscope. *Nano Lett.* **2016**, *16*, 132–137.

[162] Yuan, W. T.; Jiang, Y.; Wang, Y.; Kattel, S.; Zhang, Z. F.; Chou, L. Y.; Tsung, C. K.; Wei, X.; Li, J. X.; Zhang, X. F. et al. *In situ* observation of facet-dependent oxidation of graphene on platinum in an environmental TEM. *Chem. Commun.* **2015**, *51*, 350–353.

[163] Zhang, L. X.; Miller, B. K.; Crozier, P. A. Atomic level *in situ* observation of surface amorphization in anatase nanocrystals during light irradiation in water vapor. *Nano Lett.* **2013**, *13*, 679–684.

[164] Newton, M. A.; Belver-Coldeira, C.; Martínez-Arias, A.; Fernández-García, M. Dynamic *in situ* observation of rapid size and shape change of supported Pd nanoparticles during CO/NO cycling. *Nat. Mater.* **2007**, *6*, 528–532.

[165] Nolte, P.; Stierle, A.; Jin-Phillipp, N. Y.; Kasper, N.; Schulli, T. U.; Dosch, H. Shape changes of supported Rh nanoparticles during oxidation and reduction cycles. *Science* **2008**, *321*, 1654–1658.

[166] Yoshida, H.; Matsuura, K.; Kuwauchi, Y.; Kohno, H.; Shimada, S.; Haruta, M.; Takeda, S. Temperature-dependent change in shape of platinum nanoparticles supported on CeO_2 during catalytic reactions. *Appl. Phys. Express* **2011**, *4*, 065001.

[167] Hansen, P. L.; Wagner, J. B.; Helveg, S.; Rostrup-Nielsen, J. R.; Clausen, B. S.; Topsøe, H. Atom-resolved imaging of dynamic shape changes in supported copper nanocrystals. *Science* **2002**, *295*, 2053–2055.

[168] Uchiyama, T.; Yoshida, H.; Kuwauchi, Y.; Ichikawa, S.; Shimada, S.; Haruta, M.; Takeda, S. Systematic morphology changes of gold nanoparticles supported on CeO_2 during CO oxidation. *Angew. Chem., Int. Ed.* **2011**, *50*, 10157–10160.

[169] Jiang, Y.; Li, H. B.; Wu, Z. M.; Ye, W. Y.; Zhang, H.; Wang, Y.; Sun, C. H.; Zhang, Z. *In situ* observation of hydrogen-induced surface faceting for palladium-copper nanocrystals at atmospheric pressure. *Angew. Chem., Int. Ed.* **2016**, *55*, 12427–12430.

[170] Zhu, B. B.; Xu, Z.; Wang, C. L.; Gao, Y. Shape evolution of metal nanoparticles in water vapor environment. *Nano Lett.* **2016**, *16*, 2628–2632.

[171] Zhang, S. Y.; Plessow, P. N.; Willis, J. J.; Dai, S.; Xu, M. J.; Graham, G. W.; Cargnello, M.; Abild-Pedersen, F.; Pan, X. Q. Dynamical observation and detailed description of catalysts under strong metal-support interaction. *Nano Lett.* **2016**, *16*, 4528–4534.

[172] Tao, F.; Grass, M. E.; Zhang, Y. W.; Butcher, D. R.; Renzas, J. R.; Liu, Z.; Chung, J. Y.; Mun, B. S.; Salmeron, M.; Somorjai, G. A. Reaction-driven restructuring of Rh-Pd and Pt-Pd core–shell nanoparticles. *Science* **2008**, *322*, 932–934.

[173] Gao, F.; Wang, Y. L.; Goodman, D. W. CO oxidation over AuPd(100) from ultrahigh vacuum to near-atmospheric pressures: The critical role of contiguous Pd atoms. *J. Am. Chem. Soc.* **2009**, *131*, 5734–5735.

[174] Gao, F.; Wang, Y. L.; Goodman, D. W. CO oxidation over AuPd(100) from ultrahigh vacuum to near-atmospheric pressures: CO adsorption-induced surface segregation and reaction kinetics. *J. Phys. Chem. C* **2009**, *113*, 14993–15000.

[175] Tao, F.; Grass, M. E.; Zhang, Y. W.; Butcher, D. R.; Aksoy, F.; Aloni, S.; Altoe, V.; Alayoglu, S.; Renzas, J. R.; Tsung, C.-K. et al. Evolution of structure and chemistry of bimetallic nanoparticle catalysts under reaction conditions. *J. Am. Chem. Soc.* **2010**, *132*, 8697–8703.

[176] Wang, L.-L.; Tan, T. L.; Johnson, D. D. Configurational thermodynamics of alloyed nanoparticles with adsorbates. *Nano Lett.* **2014**, *14*, 7077–7084.

[177] Xin, H. L.; Alayoglu, S.; Tao, R. Z.; Genc, A.; Wang, C.-M.; Kovarik, L.; Stach, E. A.; Wang, L.-W.; Salmeron, M.; Somorjai, G. A. et al. Revealing the atomic restructuring of Pt-Co nanoparticles. *Nano Lett.* **2014**, *14*, 3203–3207.

[178] Wu, Y. A.; Li, L.; Li, Z.; Kinaci, A.; Chan, M. K. Y.; Sun, Y. G.; Guest, J. R.; McNulty, I.; Rajh, T.; Liu, Y. Z. Visualizing redox dynamics of a single Ag/AgCl heterogeneous nanocatalyst at atomic resolution. *ACS Nano* **2016**, *10*, 3738–3746.

[179] Inukai, J.; Tryk, D. A.; Abe, T.; Wakisaka, M.; Uchida, H.; Watanabe, M. Direct STM elucidation of the effects of atomic-level structure on Pt(111) electrodes for dissolved CO oxidation. *J. Am. Chem. Soc.* **2013**, *135*, 1476–1490.

[180] Narayanan, R.; El-Sayed, M. A. Shape-dependent catalytic activity of platinum nanoparticles in colloidal solution. *Nano Lett.* **2004**, *4*, 1343–1348.

[181] Bratlie, K. M.; Lee, H.; Komvopoulos, K.; Yang, P. D.; Somorjai, G. A. Platinum nanoparticle shape effects on benzene hydrogenation selectivity. *Nano Lett.* **2007**, *7*, 3097–3101.

[182] Johnson, W. H. On some remarkable changes produced in iron and steel by the action of hydrogen and acids. *Proc. Roy. Soc. Lond.* **1874**, *23*, 168–179.

[183] Tabata, T.; Birnbaum, H. K. Direct observations of hydrogen enhanced crack propagation in iron. *Scripta Metall.* **1984**, *18*, 231–236.

[184] Tabata, T.; Birnbaum, H. K. Direct observations of the effect of hydrogen on the behavior of dislocations in iron. *Scripta Metall.* **1983**, *17*, 947–950.

[185] Robertson, I. M.; Birnbaum, H. K. An HVEM study of hydrogen effects on the deformation and fracture of nickel. *Acta Metall.* **1986**, *34*, 353–366.

[186] Bond, G. M.; Robertson, I. M.; Birnbaum, H. K. Effects of hydrogen on deformation and fracture processes in high-ourity aluminium. *Acta Metall.* **1988**, *36*, 2193–2197.

[187] Rozenak, P.; Robertson, I. M.; Birnbaum, H. K. HVEM studies of the effects of hydrogen on the deformation and fracture of AISI type 316 austenitic stainless steel. *Acta Metall. Mater.* **1990**, *38*, 2031–2040.

[188] Hänninen, H. E.; Lee, T. C.; Robertson, I. M.; Birnbaum, H. K. *In situ* observations on effects of hydrogen on deformation and fracture of A533B pressure vessel steel. *J. Mater. Eng. Perform.* **1993**, *2*, 807–817.

[189] Zheng, S. J.; Wang, Y. J.; Zhang, B.; Zhu, Y. L.; Liu, C.; Hu, P.; Ma, X. L. Identification of $MnCr_2O_4$ nano-octahedron in catalysing pitting corrosion of austenitic stainless steels. *Acta Mater.* **2010**, *58*, 5070–5085.

[190] Zhang, B.; Wang, J.; Wu, B.; Zhou, Y. T.; Ma, X. L. Quasi-*in-situ* ex-polarized TEM observation on dissolution of MnS inclusions and metastable pitting of austenitic stainless steel. *Corros. Sci.* **2015**, *100*, 295–305.

[191] Malladi, S. R. K.; Tichelaar, F. D.; Xu, Q.; Wu, M. Y.; Terryn, H.; Mol, J. M. C.; Hannour, F.; Zandbergen, H. W. Quasi *in situ* analytical TEM to investigate electrochemically induced microstructural changes in alloys: AA2024-T3 as an example. *Corros. Sci.* **2013**, *69*, 221–225.

[192] Chenna, S.; Crozier, P. A. Operando transmission electron microscopy: A technique for detection of catalysis using electron energy-loss spectroscopy in the transmission electron microscope. *ACS Catal.* **2012**, *2*, 2395–2402.

[193] Zewail, A. H. Four-dimensional electron microscopy. *Science* **2010**, *328*, 187–193.

[194] Flannigan, D. J.; Zewail, A. H. 4D electron microscopy: Principles and applications. *Acc. Chem. Res.* **2012**, *45*, 1828–1839.

[195] Xie, D. G.; Li, S. Z.; Li, M.; Wang, Z. J.; Gumbsch, P.; Sun, J.; Ma, E.; Li, J.; Shan, Z. W. Hydrogenated vacancies lock dislocations in aluminium. *Nat. Commun.* **2016**, *7*, 13341.